https://ntrs.nasa.gov/search.jsp?R=20120013322 2019-08-30T21:33:35+00:00Z

Mon. Not. R. Astron. Soc. **000**, 1–17 (2011) Printed 4 January 2012 (MN LaTeX style file v2.2)

All-sky Observational Evidence for An Inverse Correlation between Dust Temperature and Emissivity Spectral Index

Z. Liang,[1⋆] D. J. Fixsen[2] and B. Gold[1]
[1]*Department of Physics & Astronomy, The Johns Hopkins University, 3400 N. Charles St., Baltimore, MD, 21218, USA*
[2]*University of Maryland, Goddard Space Flight Center, MD, 20771, USA*

arXiv:1201.0060v1 [astro-ph.GA] 30 Dec 2011

4 January 2012

ABSTRACT

We show that a one-component variable-emissivity-spectral-index model (the free-α model) provides more physically motivated estimates of dust temperature at the Galactic polar caps than one- or two-component fixed-emissivity-spectral-index models (fixed-α models) for interstellar dust thermal emission at far-infrared and millimeter wavelengths. For the comparison we have fit all-sky one-component dust models with fixed or variable emissivity spectral index to a new and improved version of the 210-channel dust spectra from the *COBE*-FIRAS, the $100-240$ μm maps from the *COBE*-DIRBE and the 94 GHz dust map from the *WMAP*. The best model, the free-α model, is well constrained by data at $60-3000$ GHz over 86 per cent of the total sky area. It predicts dust temperature ($T_{\rm dust}$) to be $13.7-22.7$ (±1.3) K, the emissivity spectral index (α) to be $1.2-3.1$ (±0.3) and the optical depth (τ) to range $0.6-46\times10^{-5}$ with a 23 per cent uncertainty. Using these estimates, we present all-sky evidence for an inverse correlation between the emissivity spectral index and dust temperature, which fits the relation $\alpha=1/(\delta+\omega\cdot T_{\rm dust})$ with $\delta=-0.510\pm0.011$ and $\omega=0.059\pm0.001$. This best model will be useful to cosmic microwave background experiments for removing foreground dust contamination and it can serve as an all-sky extended-frequency reference for future higher resolution dust models.

Key words: dust, extinction – infrared: ISM – submillimetre: ISM – Galaxy: general – methods: data analysis – technique: spectroscopic.

1 INTRODUCTION

An accurate model of thermal dust emission at the far-infrared and millimetre wavelengths is important for cosmic microwave background (CMB) anisotropy studies because it helps to remove one of the three major diffused foreground contaminants. In the last decade, experiments such as the *Wilkinson Microwave Anisotropy Probe* (*WMAP*, Bennett et al. 2003a) have precisely measured the angular variations in CMB signal in order to understand the global geometry and expansion of the universe. However, studying variations that are 10^{-5} the strength of the principal signal is difficult, and the removal of contaminating signals in the data needs to be done accurately. For these experiments, a dust template, such as one extrapolated from the Finkbeiner, Davis & Schlegel (1999) (FDS) study of interstellar dust in the far-infrared has been used to remove thermal dust contribution from sky measurements (Bennett et al. 2003b; Hinshaw et al. 2007; Gold et al. 2009).

Among major efforts to derive an all-sky dust model from observational data, Reach et al. (1995) use dust spectra derived from measurements of the Far Infrared Absolute Spectrophotometer (FIRAS, FIRAS Explanatory Supplement (1997)) instrument on board the *Cosmic Background Explorer* (*COBE*, Mather 1982) satellite to constrain dust models with emissivity proportional to ν^2. They found that dust emission is best described by a three-component dust model: a warm ($16-21$ K) and a cold ($4-7$ K) component that are present everywhere in the sky, and an intermediate temperature ($10-14$ K) component that exists only at the Inner Galaxy. In 1996, Boulanger et al. independently derived another set of dust spectra using the FIRAS measurements and fit it a one-component ν^2 emissivity dust model. They find that the average spectrum of dust associated with HI gas has an averaged temperature of 17.5 ± 0.2 K. In 1998, Lagache et al. used DIRBE bands at 100, 140 and 240 μm to decompose FIRAS spectra at $|b|>10^\circ$ into a cirrus and a cold component. For 61 per cent of the sky where the cold emission is negligible, they found that the cirrus had a mean temperature of 17.5 K with a dispersion of 2.5 K. For the 3.4 per cent sky where both cirrus and cold components are present, the two components are both assumed to follow a ν^2 emissivity law, with the cirrus component found to have a temperature of 17.8 ± 1.2 K, and the cold component with a temperature of 15 ± 0.8 K. A widely used dust model in CMB studies was obtained by Finkbeiner et al. (1999). Their best model (Model #8)

⋆ E-mail: zliang1@jhu.edu

© 2011 RAS

to the FIRAS dust spectra consist of two dust components: a cold component following a $\nu^{1.67}$ emissivity law with temperature at $7.7 - 13.1$ K, and a warm component following a $\nu^{2.70}$ emissivity law with temperature at $13.6 - 21.2$ K. A decade later, the Planck Collaboration (Planck Collaboration 2011a) used the *Planck*-HFI (350 μm–2mm) and IRAS 100 μm data to derive all-sky dust temperature and optical depth maps using a one-component model with emissivity proportional to $\nu^{1.8}$. They found that the median temperature of the sky at 10° above and below the Galactic plane is 17.7 K, see also Liang (2011).

This list of results highlights the diverse findings in the study of thermal dust emission at far-infrared and millimetre wavelengths. It also shows that the derived dust properties depend as much on the fitting method and the functional form of the model as on the data. With added new and more sensitive data from the *WMAP*, we now can constrain model parameters with much greater accuracy.

A second motivation for our work is to understand whether dust optical properties (Draine & Lee 1984) are the same at far-infrared and millimetre wavelengths from the perspective of empirical model fitting. That far-infrared dust emissivity follows a ν^2 power law has been widely accepted (see list above), yet the validity of such extrapolation has not been proved by theory, laboratory experiment or empirical model fitting. In fact, laboratory measurements of Agladze et al. (1996) and Mennella et al. (1998) found that emissivity of amorphous silicate and carbon grains differed from a ν^2 power law and had a significant temperature dependence. This inconsistency between observation and practice means that our understanding of dust emission in the far-infrared and millimetre is incomplete. In this work, we attempt to fill this gap by first deriving best-fitting dust models with emissivity spectral index fixed at different values and as a variable, and then comparing the quality-of-fit of these models. Based on our findings, we argue that dust emissivity differs in the far-infrared and millimetre from the optical.

A third reason for our work is to demonstrate a spatial averaging technique to increase signal-to-noise of spectra. At low intensity regions data often come with large uncertainty. If such data are used directly to constraint a model, results are highly uncertain parameters. At times this problem is treated with averaging data within a predefined sky region. This approach has the disadvantage of using a presupposed dust distribution in the derivation of a solution while figuring out the distribution is part of the research question. Here we make no assumption of the dust distribution but instead use the signal-to-noise of the data to determine the amount of spatial averaging needed for the data. The results are higher spatial resolution for regions with good signal-to-noise and less averaging for the original data set. This technique could be applied to similar problems in other areas of research.

Finally, regarding the many empirical models we now know, e.g. the ones listed above, one cannot help but ask: How do we test the validity of these models? Beside having good constraint on model parameters, are there physically motivated tests we can use to verify predictions of these models? Here, we propose one: to compare dust temperature distribution with the distribution of dust heating source at the Galactic poles. We conduct an independent and comprehensive test on all-sky one-component models, and show that all but the one-component free-α model fail this test.

The structure of our manuscript is as follows. In Section 2, we review observations by the *COBE* satellite's DIRBE and FIRAS experiments and the *WMAP* satellite that are used in our model construction. In Section 3 we detail procedures taken to deduce a new set of FIRAS dust spectra and to unify calibrations of the data sets. In Section 4, we present results and analysis from fitting one-component dust models with fixed and variable emissivity spectral index to the data. In Section 5, we compare temperature predictions of the free-α model with those of the fixed-α models and show that only the free-α model gives physically motivated predictions of dust temperature at the Galactic polar caps. We also discuss the implications of the free-α model on the inverse correlation between emissivity spectral index and dust temperature. Conclusions along with suggestions for how to use our results are presented in Section 6.

2 OBSERVATIONS

The following sections review the instruments and the data sets we used in the following analysis.

2.1 *COBE* DIRBE

The DIRBE instrument was a cryogenically cooled 10-band absolute photometer designed to measure the spectrum and angular distribution of the diffuse infrared background. It had a $0\overset{\circ}{.}7$ beam and covered the wavelength range from 1.25 to 240 μm. During its lifetime, the DIRBE achieved a sensitivity of 10^{-9} W m^{-2} sr^{-1} at most wavelengths (Boggess et al. 1992; Silverberg et al. 1993; DIRBE Explanatory Supplement 1998).

We use the 1997 "Pass 3b" Zodi-Subtracted Mission Average (ZSMA) Maps at bands 100, 140 and 240 μm. These maps measure the Galactic and extragalactic diffuse infrared emission, and have been calibrated to remove zodiacal light (zodi). They are available at the Legacy Archive for Microwave Background Data Analysis (LAMBDA)[1].

2.2 *COBE* FIRAS

The FIRAS instrument was a polarizing Michelson interferometer designed to precisely measure the difference between the CMB and a blackbody spectrum. The FIRAS had a 7° beam and covered the frequency range from $1 - 97$ cm^{-1} at 0.45 cm^{-1} resolution (Boggess et al. 1992; Fixsen et al. 1994a; FIRAS Explanatory Supplement 1997).

We derive a new set of dust spectral maps from the Destriped Sky Spectra of the Pass 4 final data release. The procedures are described in Section 3. The 210 6063-pixel maps comprise the main body of spectral information we use in model fitting.

Six types of uncertainties have been characterized by the FIRAS Team. Fixsen et al. (1994b); FIRAS Explanatory Supplement (1997); Mather et al. (1999) provide extensive instructions on how to treat each type of uncertainty. Since we build models that respond to both spectral and spatial variations of dust emission, the following analysis includes all six FIRAS uncertainties: detector noise (D), emissivity gain uncertainties (PEP), bolometer parameter gain uncertainties (JCJ), internal calibrator temperature errors (PUP), absolute temperature errors (PTP), and destriper errors (β). Section 7.10 of FIRAS Explanatory Supplement (1997) provides very helpful instructions on how to assemble the covariance matrix. For example, the D and β matrices vary only

[1] The LAMBDA Web site is http://www.lambda.gsfc.nasa.gov/

Table 1. Spectral Coverage of DIRBE, FIRAS & *WMAP*

	λ (μm)	$1/\lambda$ (cm^{-1})	ν (GHz)
DIRBE	100	100	2998
	140	71	42
	240	42	1249
FIRAS	$103-4407$	$2-97$	$68-2911$
WMAP	3189	3	94

among pixels, while the PEP, JCJ, PUP and PTP matrices differ for different frequencies. Interested readers are referred to the FIRAS Explanatory Supplement (1997) for details.

2.3 *WMAP*

The Wilkinson Microwave Anisotropy Probe was designed to determine the geometry, content and evolution of the universe by measuring temperature anisotropy of the CMB radiation. It consisted of two back-to-back offset Gregorian telescopes, and used 20 high electron mobility transistor (HEMT) based differential radiometers to measure the brightness difference between two lines of sight that were 141° apart. At five frequency bands: 23, 33, 41, 61 and 94 GHz, the *WMAP* made full sky measurements, which were analyzed by the data processing pipeline and form 13′ FWHM HEALPix[2] pixelization maps. The spin motion of the observatory and its scanning strategy symmetrized the *WMAP* beams. Beam sizes were estimated using square-root of the beam solid angle. In order of increasing frequencies, they are: 0.88, 0.66, 0.51, 0.35 and 0.22° (Jarosik et al. 2003; Page et al. 2003; Hinshaw et al. 2003; Jarosik et al. 2007; *WMAP* Five-Year Explanatory Supplement 2008; Hinshaw et al. 2009; Hill et al. 2009).

We use the dust temperature map (at 94 GHz) derived from the "base model" in *WMAP*'s Five-Year foreground modeling analysis by Gold et al. (2009). In the same study, Gold et al. used different models to account for diffused foreground emission at different *WMAP* bands, with nonthermal synchrotron, thermal bremsstrahlung, and thermal dust as the standard components and tested the possible existence of steepening synchrotron and/or spinning dust. Their likelihood analysis showed that basic model with just three main foreground components was sufficient to subtract out foregrounds from sky maps at high Galactic latitudes.

3 DATA PREPARATION

Since we want to model both spectral and spatial variations of dust emission, we unify different hardware constraints and calibration standards to ensure that different data sets are compared on an equal footing. In Section 3.1 we discuss the FIRAS data, the primary for this study. In Sections 3.2 – 3.7 we explain alignment of the DIRBE and WMAP data with the FIRAS data. The procedures on beam differences, map projections, spatial resolutions, DIRBE-FIRAS absolute calibrations, and temperature-flux conversion are applied to both signal and noise maps. Procedures on zodi zero-point corrections and FIRAS systematic errors are applied to noise maps only.

[2] For definition and applications of the HEALPix projection, refer to Górski, Hivon & Wandelt (1999), Górski et al. (2005), Calabretta & Roukema (2007) and http://healpix.jpl.nasa.gov.

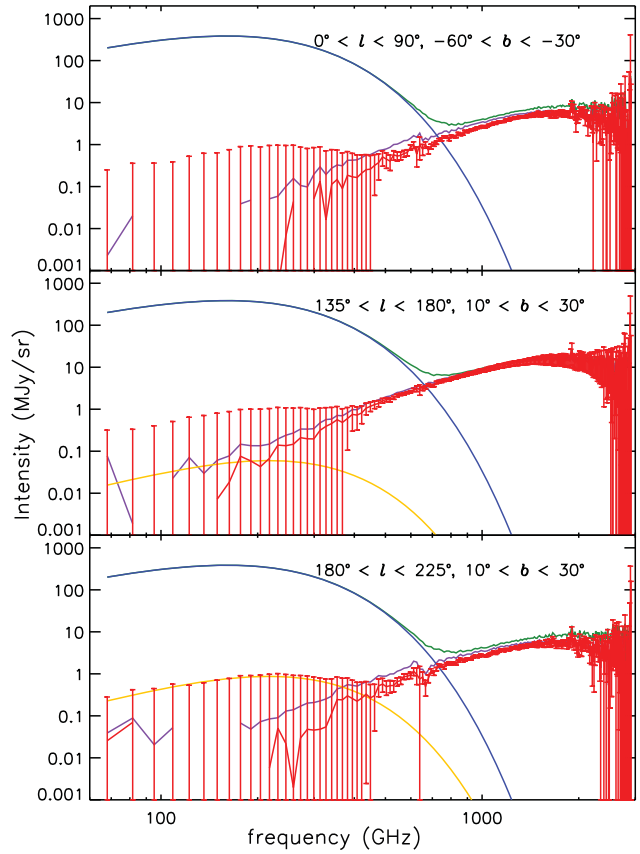

Figure 1. Examples of the new FIRAS dust spectra. Plotted in red are the new dust spectra and their error estimates; in purple are the dust spectra derived by the FIRAS team; in dark green is the total sky intensity measured by FIRAS; in blue is the CMB monopole; and in orange is the CMB dipole.

3.1 Deducing FIRAS dust spectral maps

The FIRAS dust spectra on LAMBDA exhibit a "jump" between the low- and high-band data due to an inconsistant CMB monopole temperature subtraction. In addition, the Pass 4 data were released with an early calibration, making it necessary that we derive a new set of dust spectra. In the following we describe procedures to subtract from the Destriped Sky Spectra a blackbody spectrum for the CMB, a dipole of the Earth's motion with respect to the CMB, a zodi model, and contribution from the cosmic infrared background (CIB). Examples of the new dust spectra are plotted in red in Fig. 1. For comparison, corresponding dust spectra provided by the FIRAS Team are plotted in purple.

3.1.1 CMB monopole and dipole

The CMB temperature has been extensively treated (see Mather et al. 1990; Fixsen et al. 1994b; Mather et al. 1994; Fixsen et al. 1996; Mather et al. 1999; Fixsen & Dwek 2002; Fixsen 2009). The appropreate correction for the Pass 4 data set is a 2.7278 black body spectrum.

A *WMAP*-determined dipole (Hinshaw et al. 2009) is removed from the Destriped Spectra. Specifically, $T_{\rm dipole} = 3.355$ mK and $(l, b) = (263\overset{\circ}{.}99, 48\overset{\circ}{.}26)$. Higher order variations in the CMB temperature were ignored because they are insignificant for this study.

3.1.2 Zodi

Zodi is the thermal emission and scattered light from interplanetary dust in our solar system. Kelsall et al. (1998) derived a time-dependent parametric model for its emission, and the FIRAS Team extended those results to the entire FIRAS frequency coverage (FIRAS Explanatory Supplement 1997; Fixsen & Dwek 2002). Derivation of the zodi model for FIRAS hinges on the fact that FIRAS measurements overlap with DIRBE bands at 140 and 240 μm. Therefore, the DIRBE model predictions for these two bands were coadded and fitted with a power law emissivity model and extrapolated to the frequency coverage of FIRAS. The zodi model used here is among FIRAS data products on LAMBDA. For further details of the model derivation, see Fixsen & Dwek (2002).

3.1.3 Emission lines

The FIRAS detected 18 molecular and atomic lines emitted by interstellar gas. Since the FIRAS frequency resolution is much larger than the width of each of these lines, each line profile is effectively FIRAS's instrument response to a delta function. Among these 18 detected emission lines, not all of them have a discernible presence over the full sky. Most notably are the [C II] and [N II] lines, which exhibit a distinct gradient of intensity from the centre of the Galaxy to higher latitudes. Other emission lines, though detected, are weak in most of the sky except at the Inner Galaxy. By Inner Galaxy we mean the inner Galactic disk about half the distance to the edge of the Galaxy.

Since the derivation of FIRAS line intensity maps on LAMBDA used their Galactic dust spectra, the FIRAS line intensity maps cannot be used here to remove emission line contribution. Instead, intensities of [C II] and [N II] emission are fit as parts of the overall model in the following.

3.1.4 Cosmic infrared background

The isotropic CIB signal was removed from sky spectra using results from three studies: For DIRBE measurements at 140 and 240 μm, the CIB is removed at 15 and 13 nW m^{-2} sr^{-1} respectively according to Hauser et al. (1998). For the DIRBE band at 100 μm, the CIB is removed at 25 nW m^{-2} sr^{-1}, as given in Finkbeiner et al. (2000). Notice that the Finkbeiner prediction is within the upper and lower limits estimated by the DIRBE Team. To remove the CIB from FIRAS sky spectra, the CIB model in Fixsen et al. (1998) is used.

3.2 Beam difference

The three instruments that produced the data used in this study had different beam patterns. For example, the FIRAS used a quasi-optical multimode horn antenna to collect radiation from a 7° field of view (Mather et al. 1986). The horn was designed in a trumpet bell shape to reduce response to off-axis radiation. As a result, when the beam profile was measured on the ground and in flight, it was found to have very low sidelobes over the two decades of frequency measured by FIRAS. The central portion of the beam ($\theta < 3\overset{\circ}{.}5$) is approximated by a top hat since any slight azimuthal asymmetry should have been smoothed out by the rotation of the instrument along its own axis (Mather et al. 1993) during its operation.

On the other hand, DIRBE was built with a goal to reject stray light to measure the absolute spectrum and angular distribution of the CIB. This goal was met by using a series of optical elements and baffle protections, among which the last field stop set the $0\overset{\circ}{.}7 \times 0\overset{\circ}{.}7$ instantaneous field of view for all spectral bands (Silverberg et al. 1993; DIRBE Explanatory Supplement 1998). To construct the ZSMA maps, the DIRBE Team calculated the zodiacal light intensity using the IPD model by Kelsall et al. (1998), and subtracted it off from each weekly measurement. The remaining signal was averaged over time. In this way, the ZSMA maps preserve the original $0\overset{\circ}{.}7 \times 0\overset{\circ}{.}7$ angular resolution of the sky observation.

The dust map from the *WMAP* was one of the products derived from Markov chain Monte Carlo fitting of temperature and polarization data (Gold et al. 2009). Since their analysis used the band-averaged maps that were smoothed by a 1° Gaussian beam, the dust map has the same angular resolution.

The FIRAS beam is the lowest common angular resolution achievable among all three data sets, so the higher resolution DIRBE and *WMAP* maps need to be convolved with the FIRAS beam to make them all 7° maps. Additionally, since Fixsen et al. (1997b) found that the FIRAS beam was elongated in the scan direction by $2\overset{\circ}{.}4$, that pattern is matched in the degraded DIRBE and *WMAP* maps by convolving those data with an effective FIRAS beam.

3.3 Map projection and spatial resolution

Both DIRBE and FIRAS maps are organized in *COBE* quadrilateralized spherical cube format (quad-cube, Chan & O'Neill 1975, O'Neill & Laubscher 1976, White & Stemwedel 1992, and Calabretta & Greisen 2002). While the DIRBE maps are in quad-cube resolution level 9 (res9, $19\overset{\rm m}{.}43$ per pixel), the FIRAS maps are in quad-cube resolution level 6 (res6, $2\overset{\circ}{.}59$ per pixel). Different from the FIRAS and the DIRBE maps, the *WMAP* dust map is in HEALPix (Górski, Hivon & Wandelt 1999, Górski et al. 2005, and Calabretta & Roukema 2007) resolution level 6 (res6, $54\overset{\rm m}{.}97$ per pixel). One way to reconcile these different formats and spatial resolutions is to carry out analysis in *COBE* quad-cube res6. This decision is made to retain maximum amount of information contained in the original data sets and achieve the highest common resolution possible.

As a result, DIRBE maps were re-binned to res6; the *WMAP* dust map was first converted into a quad-cube res9 map and then re-binned to res6. During *WMAP*'s dust map conversion, we took the following steps to ensure that no excessive artificial noise was introduced to the final map: We compared the original HEALPix-projection map with the re-binned quad-cube-projection map, and found that 98.6 per cent of the 49,152-coordinate pairs sampled gave no difference between the quad-cube and the HEALPix values. When there was a difference, the maximum was 0.0059 mK, which amounted to a 0.11 per cent noise increase for the original HEALPix map.

3.4 Gradient correction

The FIRAS dust maps are based on coadding interferograms, so their values are generally not at the defined centre of map pixels. This positional difference requires an additional correction step to prepare the quad-cube res6 DIRBE and WMAP maps. Details of this technique are described in Fixsen et al. (1997b). In summary, a second-degree surface function is fit to the intensity and location information of a pixel and its immediate neighbors in one of the converted maps. This function is then used to predict emission at the FIRAS mean position for that particular pixel. Overall, a 5 per cent rms correction is applied to each of the DIRBE maps at 100, 140 and 240 μm and to the *WMAP* dust map.

3.5 Color correction

In accordance with the *IRAS* convention (IRAS Explanatory Supplement 1988), DIRBE photometric measurements were reported in MJy sr^{-1} at nominal wavelengths, assuming the source spectrum to be $\boldsymbol{\nu} \cdot \boldsymbol{I}_{\boldsymbol{\nu}} = \mathrm{constant}$. Since each DIRBE band has a much wider bandwidth than a FIRAS channel, spectral shape could have changed enough that at the nominal wavelength the real intensity is significantly different from the normalized intensity. As a result, we include color corrections in the overall model, i.e., model predictions are compared with DIRBE measurements using the relation $\boldsymbol{I}_{\boldsymbol{\nu},\,\mathrm{model}} = K\,\boldsymbol{I}_{\boldsymbol{\nu},\,\mathrm{DIRBE}}$, where K is the color correction factor defined as

$$K = \frac{\int (\boldsymbol{I}_{\boldsymbol{\nu}}/I_{\nu_0})_{\mathrm{actual}} \cdot \boldsymbol{R}_{\boldsymbol{\nu}}\,\mathrm{d}\,\nu}{\int (\nu_0/\boldsymbol{\nu})_{\mathrm{quoted}} \cdot \boldsymbol{R}_{\boldsymbol{\nu}}\,\mathrm{d}\,\nu}\,. \tag{1}$$

In this equation, $\int (\boldsymbol{I}_{\boldsymbol{\nu}}/I_{\nu_0})_{\mathrm{actual}}$ is the specific intensity of the sky normalized to the intensity at frequency ν_0, and $\boldsymbol{R}_{\boldsymbol{\nu}}$ is DIRBE relative system response at frequency $\boldsymbol{\nu}$. The values of $\boldsymbol{R}_{\boldsymbol{\nu}}$ are documented in DIRBE Explanatory Supplement (1998) Section 5.5.

3.6 DIRBE uncertainties

The DIRBE photometric system was maintained to ~ 1 per cent accuracy by monitoring the internal stimulator during 10 months of cryogenic operation and observing the bright stable celestial sources during normal sky scans. It was absolutely calibrated against Sirius, NGC7027, Uranus and Jupiter. Among different types of uncertainties identified by the DIRBE Team, those relevant to this work are standard deviations of intensity maps, detector gain and offset uncertainties, and zodi model uncertainties (Hauser et al. 1998; Kelsall et al. 1998; Arendt et al. 1998). For bands 8–10, respectively, the detector gains are: 0.135, 0.106 and 0.116 nW m^{-2} sr^{-1}; detector offsets are 0.81, 5 and 2 nW m^{-2} sr^{-1}; and zodi model uncertainties are: 6, 2.3 and 0.5 nW m^{-2} sr^{-1} (Arendt et al. 1998). The process of re-binning the high resolution DIRBE maps into FIRAS resolution affects only the standard deviations of the original maps. The final uncertainty is the quadrature sum of the individual noise components.

3.7 Temperature-intensity conversion

Foreground maps of the *WMAP* production are reported in antenna temperature, T_A, in mK. On the other hand, maps produced by the DIRBE and the FIRAS Teams are reported in spectral intensity, I_ν, in MJy sr^{-1}. In the following analysis, the *WMAP* dust map is converted into flux density values following $I_\nu = 2\,(\nu/c)^2\,k\,T_A$, where ν is the effective frequency (93.5 GHz) of the dust map (Gold et al. 2009; Jarosik et al. 2003), and k is Boltzmann's constant.

4 RESULTS AND ANALYSIS

4.1 Overview of model fitting strategy

The thermal emission of a dust grain is described by a modified blackbody function:

$$\boldsymbol{I}_{\mathrm{dust}}(\boldsymbol{\nu}) = \tau\,\boldsymbol{\epsilon}_{\boldsymbol{\nu}} \cdot \boldsymbol{B}_{\boldsymbol{\nu}}(T_{\mathrm{dust}})\,,$$

where $\boldsymbol{B}_{\boldsymbol{\nu}}(T_{\mathrm{dust}})$ is the blackbody spectrum at temperature T_{dust}, $\boldsymbol{\epsilon}_{\boldsymbol{\nu}} = (\boldsymbol{\nu}/\nu_0)^{\alpha}$ is the emissivity with spectral index α, and τ is the optical depth normalized to frequency $\nu_0 = 900$ GHz.

In addition to measuring thermal dust emission, the prepared FIRAS spectra retain contributions from [C II] and [N II] emission, due to the lack of precise all-sky templates. As a result, two emission lines are modeled at the same time with the dust:

$$\boldsymbol{I}_{[\mathrm{C\,II}]}(\boldsymbol{\nu}) = [\mathrm{C\,II}]_{\,\mathrm{intensity}}\;\boldsymbol{f}_{[\mathrm{C\,II}]}(\boldsymbol{\nu})\,,$$

and

$$\boldsymbol{I}_{[\mathrm{N\,II}]}(\boldsymbol{\nu}) = [\mathrm{N\,II}]_{\,\mathrm{intensity}}\;\boldsymbol{f}_{[\mathrm{N\,II}]}(\boldsymbol{\nu})\,,$$

where $\boldsymbol{f}(\boldsymbol{\nu})$ is the synthetic line profile determined by FIRAS response to a delta-function signal. Together, the full model has the form

$$\boldsymbol{I}_{\mathrm{total}} = \boldsymbol{I}_{\mathrm{dust}} + \boldsymbol{I}_{[\mathrm{C\,II}]} + \boldsymbol{I}_{[\mathrm{N\,II}]}\,. \tag{2}$$

Each full model is fit to the data by minimizing a three-part χ^2, with each part corresponding to one of the three data sets:

$$\chi^2 = \chi^2_{\mathrm{DIRBE}} + \chi^2_{\mathrm{FIRAS}} + \chi^2_{\mathrm{WMAP}}\,, \tag{3}$$

where

$$\chi^2_{\mathrm{instrument}} = \sum_{i,j} (\boldsymbol{I}_{\mathrm{obs}} - \boldsymbol{I}_{\mathrm{mdl}})_i\;(\mathbf{M}^{-1})_{ij}\;(\boldsymbol{I}_{\mathrm{obs}} - \boldsymbol{I}_{\mathrm{mdl}})_j\,, \tag{4}$$

Here, $\boldsymbol{I}_{\mathrm{obs}}$ is the observed spectral intensity, $\boldsymbol{I}_{\mathrm{mdl}}$ is the model prediction, and $\mathbf{M}$ is the covariance matrix of the respective data set.

In the following sections, we fit one-component dust models to spectra of fixed (Section 4.2) and different (Section 4.3) size sky regions. In the former case, spectra retain the 7° angular size of FIRAS pixels; in the latter case, the 7° spectra are averaged by various amounts to increase signal-to-noise of the final spectra. Chi-square per degree of freedom values, χ^2_{dof}, are used to assess the quality-of-fit of a model to each spectrum. In particular, the one-component fixed-α models have $214 - 4 = 210$ degrees of freedom. Adopting a 10 per cent probability cut-off for acceptable models, it corresponds to a $\chi^2_{\mathrm{dof}} \leqslant 1.13$. The free-$\alpha$ model has 209 degrees of freedom and its 10 per cent probability cutoff is $\chi^2_{\mathrm{dof}} \leqslant 1.13$.

4.2 Fitting spectra of 7° sky regions

We fit one-component models with fixed α in the range $1.4 - 2.6$ at 0.1 increment to the spectrum at each 7° pixel. The fits have acceptable values ($\chi^2_{\mathrm{dof}} \leqslant 1.13$) over most of the sky except at the Galactic plane.

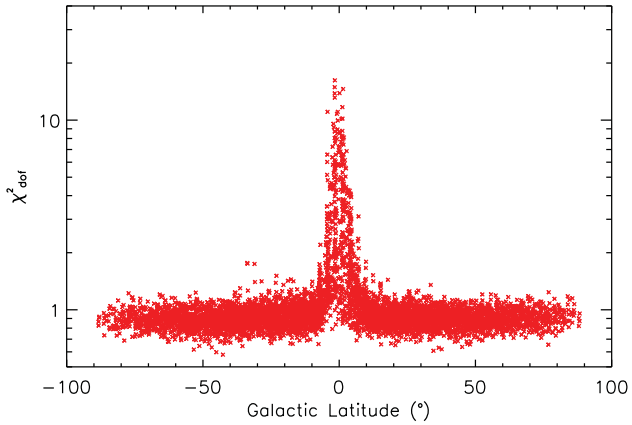

Figure 2. $\chi^2_{\rm dof}$ vs. Galactic latitude. The value of $\chi^2_{\rm dof}$ is obtained from fitting one-component $\alpha = 2.0$ model to 7° spectra covering 98.68 per cent area of the full sky where FIRAS data are available. This plot shows that most fits at $|b| \gtrsim 10°$ have a $\chi^2_{\rm dof} \sim 1$, and fits at $|b| \lesssim 10°$ have a $\chi^2_{\rm dof} > 1$.

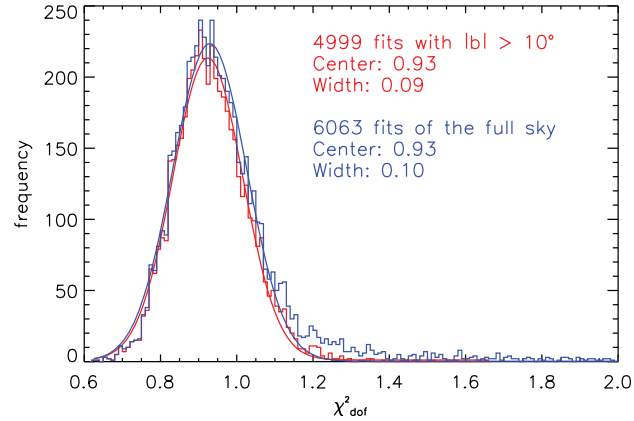

Figure 3. $\chi^2_{\rm dof}$ distributions of the 7° fits using one-component $\alpha = 2.0$ model. The red distribution includes only pixels at Galactic latitudes $|b| > 10°$; the blue distribution includes all 6063 pixels at all Galactic latitudes. Best-fitting parameters of the Gaussians are printed in respective colors. Both $\chi^2_{\rm dof}$ distributions are well approximated by a Gaussian, which means that there is no apparent systematic bias in the fits. That the distributions center at 0.93 means that errors in the data are slightly overestimated, and the widths of the distributions are as expected (0.1) for a distribution of random data with 210 degrees of freedom.

4.2.1 *Quality-of-fit of models*

As an example, Fig. 2 presents $\chi^2_{\rm dof}$ as a function of Galactic latitude for the $\alpha = 2.0$ model. It shows that most fits at $|b| \gtrsim 10°$ have $\chi^2_{\rm dof} \approx 1$, and fits at $|b| \lesssim 10°$ have a $\chi^2_{\rm dof} \gg 1$. Fig. 3 compares the distribution of $\chi^2_{\rm dof}$ at $|b| \gtrsim 10°$ with the distribution of $\chi^2_{\rm dof}$ for the entire sky. Both distributions are well approximated by a Gaussian, an indication that the fits don't have a significant systematic bias. The widths of the distributions are as expected (0.1) for a distribution of random data with 210 degrees of freedom. That the distributions center at 0.93 means that statistical errors of the data are slightly overestimated by $\sim 7\%$, and that the $\chi^2_{\rm dof}$ cutoff is really at ~ 1.21 with a probability of $< 10\%$. Because the uncertainties of the FIRAS data include some systematic effects, we do not feel at liberty to reduce the uncertainty. Based on the $\chi^2_{\rm dof} \leqslant 1.13$ cut, the model is a good fit to the data over 87 per cent of the full sky area, but is rejected by the data at the Galactic plane.

Readers interested in the best-fit parameters ($T_{\rm dust}$, τ, [C II] and [N II] intensities), their uncertainties and correlations for each of the aforementioned α models are referred to the author's PhD thesis (Liang 2011).

4.2.2 *Dependence of best-fitting parameters on the signal-to-noise of data*

Figs. 4 and 5 present $\chi^2_{\rm dof}$, $T_{\rm dust}$ and τ of the best-fitting α models for two spectra: one has high signal-to-noise (HSN) and is at a low Galactic latitude, and the other one has low signal-to-noise (LSN) and is at a high Galactic latitude. In both cases, the $\chi^2_{\rm dof}$ vs. α plots show that models with a wide range of different α values can fit the data well. In the HSN case, a curve fit to $\chi^2_{\rm dof}$ as a function of α is a concave up parabola, with the minimum $\chi^2_{\rm dof} = 0.89$ at $\alpha = 1.8$. The difference between $\chi^2_{\rm dof}$ at $\alpha = 1.8$ and that at $\alpha = 2.0$ is $\Delta\chi^2_{\rm dof} = 0.01$. At 210 degrees of freedom, this means a $\Delta\chi^2$ of ~ 2.1, which is a 2-sigma difference. In the LSN case, the best-fitting curve to $\chi^2_{\rm dof}$ vs. α is a much flatter parabola over $1.4 \leqslant \alpha \leqslant 2.3$ with the minimum $\chi^2_{\rm dof} = 0.80$ at $\alpha = 1.6$. The difference between $\chi^2_{\rm dof}$ at $\alpha = 1.8$ and $\alpha = 2.0$ is ~ 0.002.

Although models with different α have only a small difference in $\chi^2_{\rm dof}$, the best-fitting $T_{\rm dust}$ and τ are different significantly in the HSN case: At $\alpha = 2.0$, the best-fitting dust temperature is $T_{\rm dust} \sim 17.5 \pm 0.26$ K, compared to $T_{\rm dust} \sim 18.5 \pm 0.28$ K at $\alpha = 1.8$. This difference in temperature is larger than the sum of their errors. Similarly, the difference in τ of the two α models is larger than the sum of their errors. On the contrary, in the LSN case, the difference in the best-fitting $T_{\rm dust}$ and τ of $\alpha = 1.8$ and $\alpha = 2.0$ models are well within the uncertainties of the respective parameters.

These results demonstrate the sensitivity of the fits to measurement errors. The existence of measurement noise inevitably causes a high degree of degeneracy between the emissivity spectral index and the dust temperature in the fits. While it is difficult to break this degeneracy, high signal-to-noise data help. Fitting data with high signal-to-noise results in well constrained parameters, which means that the choice of an α model can cause statistically significant differences in the predictions of these parameters. On the other hand, fitting low signal-to-noise spectra results in small difference in $\chi^2_{\rm dof}$ and large error bars of the best-fit parameters, and so is not possible to differentiate models with different fixed values of α. This is demonstrated in Fig. 6, which shows that the 68 and 95 per cent confidence contours of a HSN fit enclose much smaller regions in the T-α space than those of a LSN fit.

Figs. 7 shows sky maps of α and $T_{\rm dust}$ that correspond to the minimum-$\chi^2_{\rm dof}$ model among all models tested at each pixel. Overall, the two maps are noisy, which is a result of insufficient signal-to-noise in the data that prevents setting tight constraints on the best-fitting parameters. More specifically, both maps show greater consistency in value at low latitudes and more fluctuations around the Galactic poles. That consistent values appear in the region surrounding the Inner Galaxy is reasonable because star formation takes place in the Galactic disk and at the bulge, and star formation is the most important heat source for dust. That large fluctuations appear near the poles, on the other hand, has to do with low signal-to-noise data in these regions compared to those measured at lower latitudes. This happens because few dust grains exist at high latitudes, and they do not emit as strongly as those close to the Galactic disk.

Since low signal-to-noise data cannot give adequate constraint to model parameters and exacerbates the degeneracy between dust

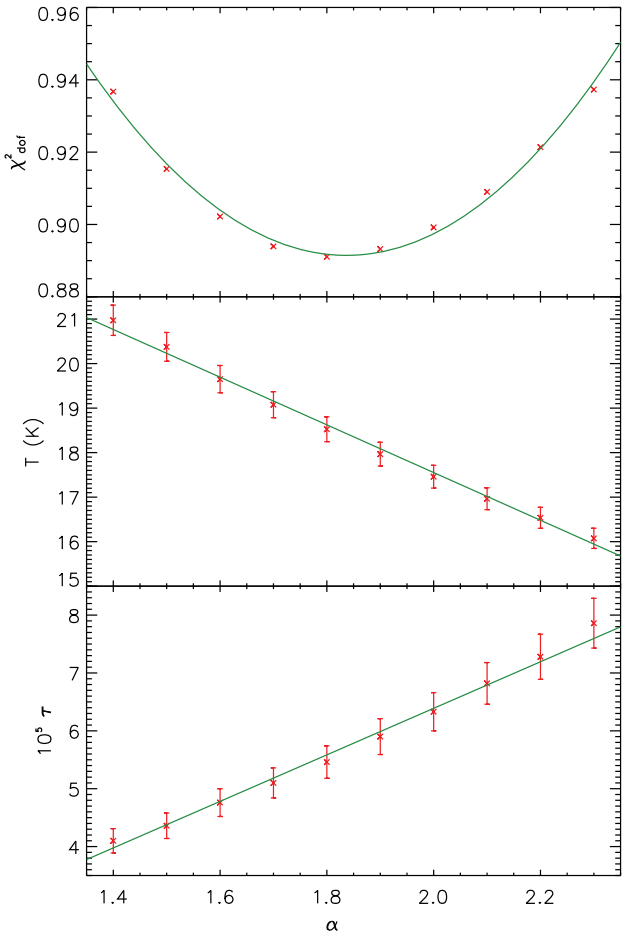

Figure 4. $\chi^2_{\rm dof}$, $T_{\rm dust}$ and τ as a function of α. Each data point on the $T_{\rm dust}$ and τ plots is the best-fitting value of the corresponding one-component fixed-α model to the 7° spectrum measured in the direction $l = 63\overset{\circ}{.}78$ and $b = -11\overset{\circ}{.}53$. This set of plots serves as an example of high signal-to-noise fits. The green curve fits the best-fitting values as a function of α. In particular, the plot of $\chi^2_{\rm dof}$ shows that the model with $\alpha = 1.8$ is a better fit to the data than the model with $\alpha = 2.0$. The small error bars of $T_{\rm dust}$ and τ show that the choice of an α model can cause statistically significant difference in the predictions of these parameters.

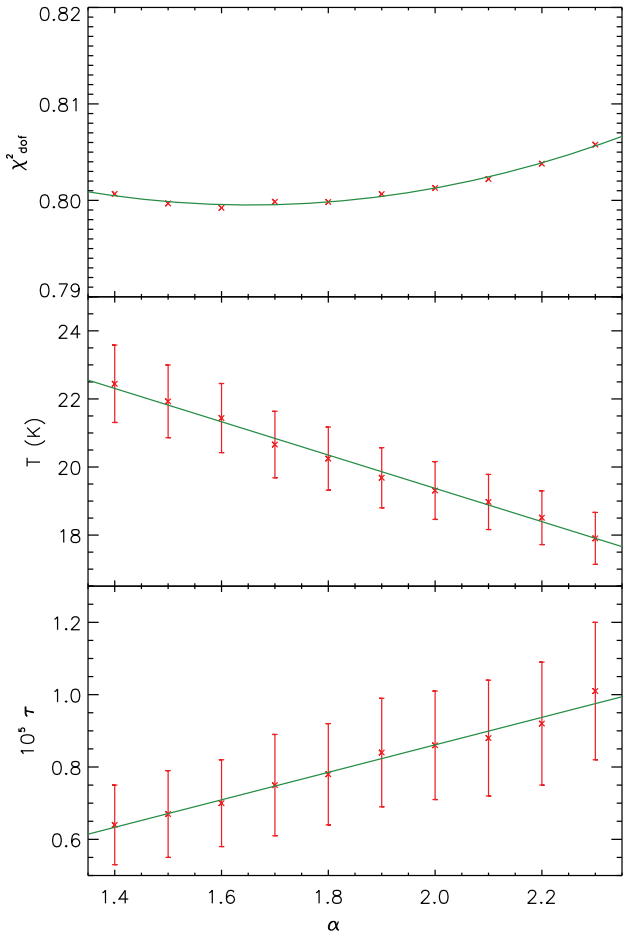

Figure 5. $\chi^2_{\rm dof}$, $T_{\rm dust}$ and τ as a function of α. Each data point on the $T_{\rm dust}$ and τ plots is the best-fitting value of the corresponding one-component fixed-α model to the 7° spectrum measured in the direction $l = 254\overset{\circ}{.}32$ and $b = 65\overset{\circ}{.}08$. This set of plots serves as an example of low signal-to-noise fits. The green curve fits the best-fitting values as a function of α. Because of the small difference in $\chi^2_{\rm dof}$ and large errors in the model parameters, fit results cannot differentiate models at different fixed values of α.

temperature and spectral index, in order to construct the best dust model, we need to find ways to increase the signal-to-noise of the data.

4.3 Fitting averaged spectra of different-size sky regions

Taking average of the high-latitude spectra based on latitudinal or longitudinal divisions of the sky can tighten the constraint on model parameters since it increases the signal-to-noise of the data. However, such divisions are based on our expectations of the distribution of Galactic dust. Since our knowledge is not complete, the divisions are not optimal. In our experiments (Liang 2011), χ^2 of regional fits are much higher than χ^2 of fits to the individual 7° spectra that comprise the regional averages. Since larger sky regions include different types of dust emission spectra, the steep increase in χ^2 value means that the averaging has achieved a sufficient signal-to-noise ratio, so spectral variation becomes statistically important. In order to preserve information on spectral variation in the model, the amount of spatial averaging needs to be adjusted according to the signal-to-noise of the data.

One way to increase the signal-to-noise of high-latitude spectra and to best preserve intrinsic variations in the signal detected from different sky directions is to base the amount of spectral averaging on signal-to-noise of the averaged spectrum. Starting with the base level, where a pixel's own spectrum is used to fit a model, if the fit does not give well constrained parameters due to inadequate signal-to-noise, the procedure goes on to fit the average of the original spectrum and its eight immediate neighbors. This process of involving more of the adjacent spectra to form a new average goes on until the derived parameters are sufficiently constrained. In this way, results from fits done at the base level have a spatial resolution of 6.71 $\square^2$. At the next level, results have a spatial resolution of 60.37 $\square^2$, and so on.

4.3.1 $T_{\rm dust}/\delta T_{\rm dust}$ *constraint on fixed-α models*

All-sky one-component fixed-α models with α in the range $1.4 - 2.6$ and lower limit of $T_{\rm dust}/\delta T_{\rm dust}$ at 5, 10, 20 and 40 are obtained

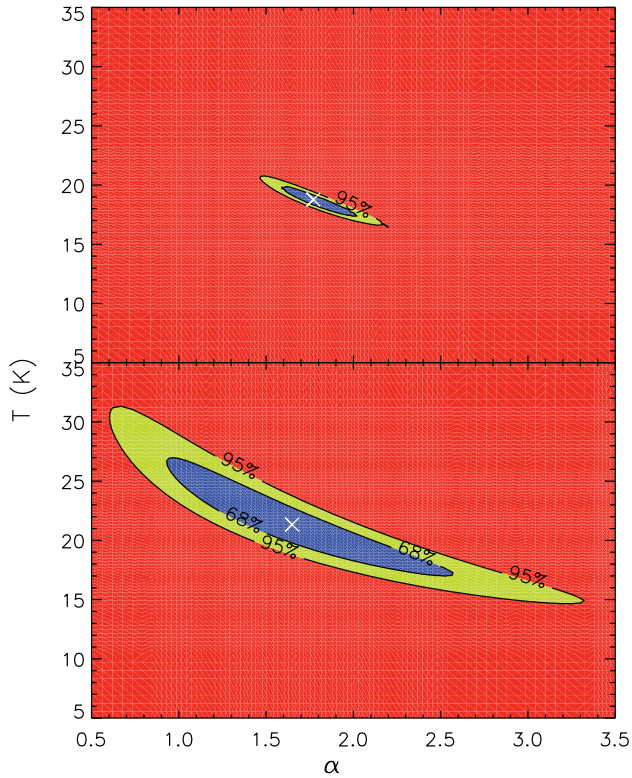

Figure 6. 68 and 95 per cent probability contours in the $T_{\rm dust}$-α space for a high signal-to-noise spectrum (upper plot, measured in the direction $l = 63\overset{\circ}{.}78$ and $b = -11\overset{\circ}{.}53$) and a low signal-to-noise spectrum (lower plot, $l = 254\overset{\circ}{.}32$ and $b = 65\overset{\circ}{.}08$). In both plots, the white cross represents location of the minimum χ^2; the blue area is the 68 per cent confidence region; and the green area is the 95 per cent confidence region. These plots demonstrate the effect of measurement noise on the degeneracy between α and $T_{\rm dust}$ in spectral model fitting. For the high signal-to-noise spectrum (upper plot), the 68 per cent confidence region is at $1.7 < \alpha < 1.9$ and 17.9 K $< T_{\rm dust} < 19.5$ K; for the low signal-to-noise spectrum (lower plot), the 68 per cent confidence region has a much wider extent, at $1.2 < \alpha < 2.2$ and 18.5 K $< T_{\rm dust} < 24.7$ K.

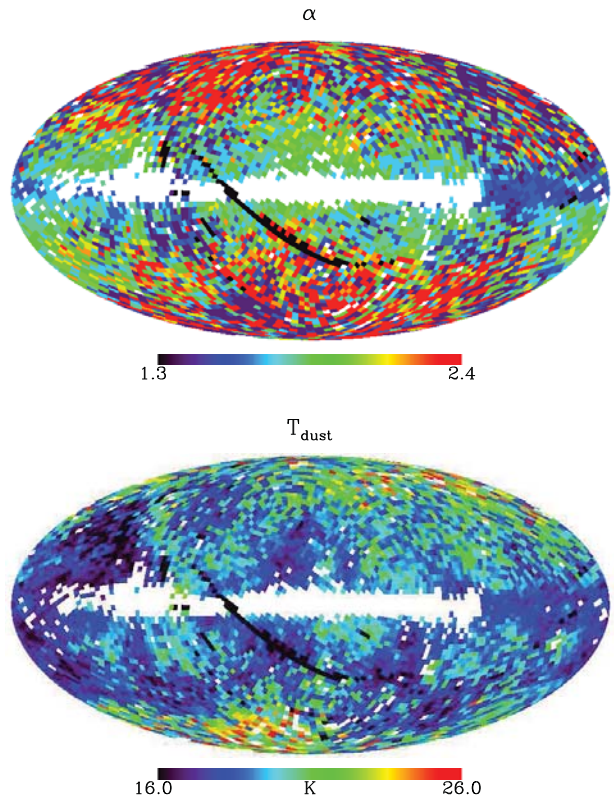

Figure 7. Sky maps of α and $T_{\rm dust}$. At each pixel the value comes from the 7° fit with the minimum $\chi^2_{\rm dof}$ among all one-component fixed-α fits in the range $1.4 \leqslant \alpha \leqslant 2.3$ at 0.1 increment. These maps are Mollweide projections of the Galaxy in Galactic coordinates. The centre of each map is the Galactic centre. The upper and lower ends of the minor axis are $+90°$ and $-90°$ latitudes respectively, and the left and right ends of the major axis represent $+180°$ and $-180°$ longitudes respectively. Both maps are noisy, particularly so at high latitudes. Pixels that correspond to fits with a χ^2 less than 10 per cent probability are masked in white. The group of black pixels that slant from the centre of the upper left quadrant (North Ecliptic Pole, NEP) to the centre of the lower right quadrant (South Ecliptic Pole, SEP) are positions where FIRAS did not provide data.

separately. In general, one-component fixed-α models with different lower limits on the $T_{\rm dust}/\delta T_{\rm dust}$ values can fit most spectra except those at the Galactic plane. A more restricted lower limit on the $T_{\rm dust}/\delta T_{\rm dust}$ values requires a greater amount of spatial averaging which stresses the dust model and causes $\chi^2_{\rm dof}$ around the Galactic poles to increase in value. The upper plot of Fig. 8 demonstrates this relation by plotting $\chi^2_{\rm dof}$ as a function of Galactic latitude for the case of $\alpha = 2.0$. Note that $\chi^2_{\rm dof}$ of high-latitude ($|b| > 60°$) fits move from $0.7 - 1.0$ to $0.8 - 1.3$ as lower limit on $T_{\rm dust}/\delta T_{\rm dust}$ starts with none and increases to 40.

Histograms of the all-sky collections of $\chi^2_{\rm dof}$ for different limits on $T_{\rm dust}/\delta T_{\rm dust}$ are presented in the lower plot of Fig. 8. The three histograms for $T_{\rm dust}/\delta T_{\rm dust} \geqslant 5$, 10 and 20, in the shape of a Gaussian, peak at 0.93, 0.94 and 0.96 respectively, and they all have a width of 0.10. The histogram for $T_{\rm dust}/\delta T_{\rm dust} \geqslant 40$ peaks at 1.00, has a width of 0.12 and a thick tail in the range $1.2 < \chi^2_{\rm dof} < 1.4$. This shows that the demand for a 40-times lower limit on $T_{\rm dust}/\delta T_{\rm dust}$ has put too much stress on the model.

Imposing a more stringent limit on $T_{\rm dust}/\delta T_{\rm dust}$ leads to a variety of spatial resolutions in each all-sky collection of fits. A more stringent requirement on $T_{\rm dust}/\delta T_{\rm dust}$ means lower spatial resolutions for fits at high latitudes. For one-component $\alpha = 2.0$ model with $T_{\rm dust}/\delta T_{\rm dust} \geqslant 5$, only 0.59 per cent of the total sky area require fits with a 60.37 $\square^2$ resolution instead of the default 6.71 $\square^2$. For a 10 per cent constraint on $T_{\rm dust}$, 0.47 per cent area of the full sky require fits to be at 167.70 $\square^2$ resolution, 7.24 per cent at 60.37 $\square^2$ resolution, and the rest at 6.71 $\square^2$ resolution. A balance between having adequate constraint on parameters, preserving as many valid models as possible, and keeping regional sizes low can be achieved at the $T_{\rm dust}/\delta T_{\rm dust} \geqslant 10$ level.

A plot of $\chi^2_{\rm dof}$ distributions for 13 all-sky fixed-α models with α in the range $1.4 - 2.6$ at 0.1 increment and satisfy $T_{\rm dust}/\delta T_{\rm dust} \geqslant 10$ is presented in Fig. 9. The high-χ^2 tails of these distributions show that models with the largest (2.6) and smallest (1.4) values of α have more fits with large $\chi^2_{\rm dof}$. We present a specific comparison of the $\chi^2_{\rm dof}$ excess for these all-sky models in the lower plot of Fig. 9. This plot shows that the all-sky $\alpha = 1.7$ model is the best because it can fit the largest amount of data (87.6 per cent area of the full sky). Fig. 10 presents sky maps of $\chi^2_{\rm dof}$, spatial resolution, dust temperature, optical depth, and the signal-to-noise of parameters from fitting the one-component $\alpha = 1.7$ model. Each of the 6063 fits presented there satisfies the $T_{\rm dust}/\delta T_{\rm dust} \geqslant 10$ requirement with the least amount of spatial averaging. In the pa-

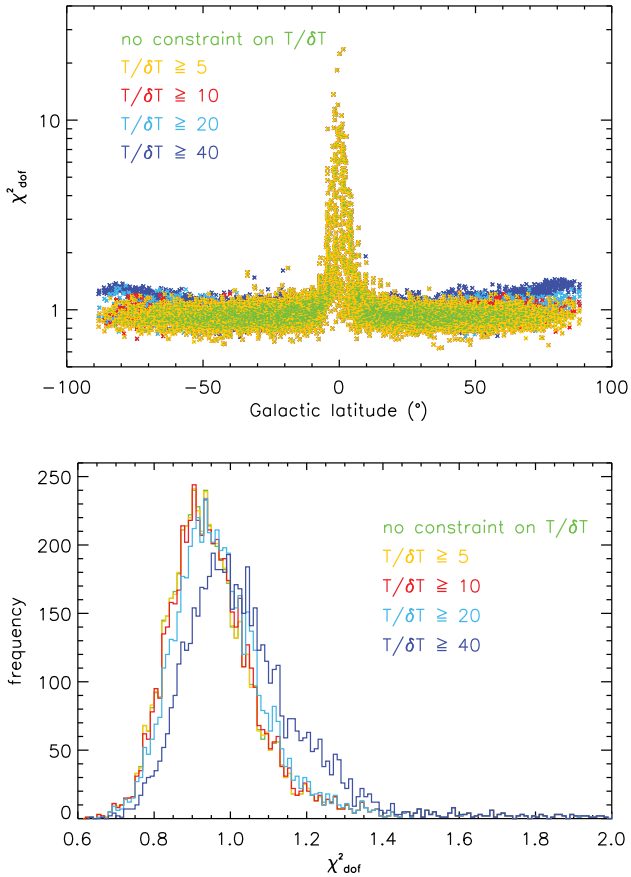

Figure 8. $\chi^2_{\rm dof}$ vs. Galactic latitude (upper) and $\chi^2_{\rm dof}$ distributions (lower) of the all-sky one-component $\alpha = 2.0$ fits that satisfy $T_{\rm dust}/\delta T_{\rm dust} \geqslant$ 5, 10, 20 and 40, respectively. With more restrictive $T_{\rm dust}/\delta T_{\rm dust}$ requirements, $\chi^2_{\rm dof}$ of high-latitude ($|b| > 60°$) fits migrate from the range $0.7 - 1.0$ to the range $0.8 - 1.3$.

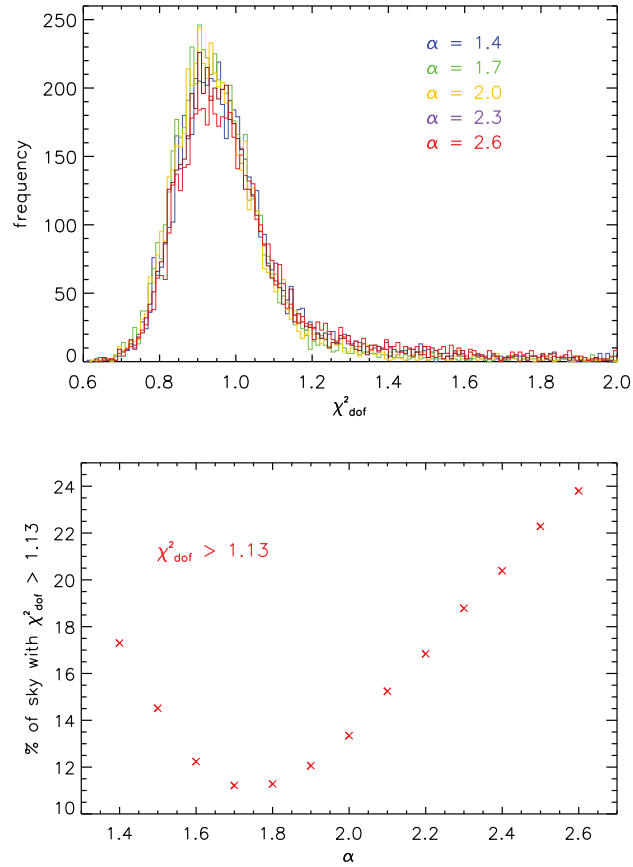

Figure 9. Upper: $\chi^2_{\rm dof}$ distributions of the best-fitting one-component fixed-α models with α in the range 1.4 – 2.6 at 0.3 increment and satisfy $T_{\rm dust}/\delta T_{\rm dust} \geqslant 10$. Lower: Percentage area of the full sky that cannot be fit by a one-component model with fixed emissivity spectral index ($\chi^2_{\rm dof}$ cutoff corresponds to 10 per cent probability). This plot shows that $\alpha = 1.7$ models can fit the largest amount of data (87.6 per cent area of the full sky).

rameter maps, if a fit has less than 10 per cent χ^2 probability (i.e., $\chi^2_{\rm dof} > 1.13$ for 210 degrees of freedom), then its corresponding pixel is masked in white. Fit results for other α models at different levels of constraint on $T_{\rm dust}/\delta T_{\rm dust}$ are provided in the first author's PhD thesis (Liang 2011).

4.3.2 $\alpha/\delta\alpha$ constraint on a free-α model

We apply a similar strategy to constrain fits that use a free-α model. Instead of the signal-to-noise of the dust temperature, we now use signal-to-noise of the emissivity spectral index to gauge the amount of spectral averaging. As an example, we present sky maps of the best-fitting parameters and their signal-to-noise for the free-α model with $\alpha/\delta\alpha \geqslant 10.0$ in Fig. 11.

Notice that the current dust temperature map has more consistent values at high latitudes near the Galactic poles than that obtained from the 7°-pixel fits in Fig. 7. The uncertainty of $T_{\rm dust}$ is less than 7.4 per cent as a result of the constraint on $\alpha/\delta\alpha$, and the uncertainty of τ has a maximum of 23.25 per cent. The spatial resolution of these fits are presented in an all-sky map in Fig. 11 and summarized in Table 2.

The upper panel in Fig. 12 compares $\chi^2_{\rm dof}$ distributions of fits that use no constraint on any parameter and those that satisfy $\alpha/\delta\alpha \geqslant 5.0$, 6.7 and 10.0. It shows that the shape of the $\chi^2_{\rm dof}$ distributions resemble a Gaussian and the constrained distributions all centre around 0.95. This means that there is no apparent systematic bias in the fits and the error estimates for the data is about right.

The plot of $\chi^2_{\rm dof}$ vs. Galactic latitude, lower panel of Fig. 12, shows that at latitudes $|b| < 10°$, $\chi^2_{\rm dof}$ continues to be $\gg 1$ as is the case of fitting all-sky one-component fixed-α models. At high latitudes, $\chi^2_{\rm dof}$ do not flare up with increasing constraint on $\alpha/\delta\alpha$, as oppose to that which happens when $T_{\rm dust}/\delta T_{\rm dust}$ requirements are imposed on a fixed-α model. It confirms our expectation that the free-α model is more adept at fitting various spectral shapes.

Fig. 13 presents distributions of α and $T_{\rm dust}$ of one-component free-α fits that use no constraint on any parameter and those that satisfy $\alpha/\delta\alpha \geqslant 5.0$, 6.7 and 10.0. The centres of the distributions are at 1.80, 1.83, 1.85 and 1.88, respectively. This plot shows that the $\alpha/\delta\alpha$ requirement has the effect of moving α from below 1.5 to higher values. With even a moderate amount of constraint on $\alpha/\delta\alpha$, the range of α values quickly reduces to between 1 and 3, an indication that values outside of this range are rare in nature.

Also shown in Fig. 13, the $T_{\rm dust}$ distributions do not peak at a single value. Instead, there is a range of most popular temperatures between 17 and 20 K. Compared to the unconstrained case, the $\alpha/\delta\alpha$ requirement smooths out the high-temperature points and effectively replaces them with values at or below 20 K.

The amounts of constraint on dust temperature, optical depth

Table 2. Spatial resolution of the one-component free-α fits with $\chi^2_{\rm dof} \leqslant 1.13$

Level	Regional size of fits ($\square^2$)	Percentage of the full sky at a regional average $\alpha/\delta\alpha \geqslant 5.0$	$\alpha/\delta\alpha \geqslant 6.7$	$\alpha/\delta\alpha \geqslant 10.0$
1	6.71	40.01	30.63	22.09
2	60.43	23.14	24.53	22.51
3	167.86	11.87	11.07	10.60
4	329.00	4.61	8.59	6.41
5	543.86	3.53	3.48	5.53
6	812.44	2.18	2.78	4.62
7	1134.73	1.01	2.12	3.30
8	1510.73		1.92	2.59
9	1940.45		1.22	2.23
10	2423.88			2.08
11	2961.03			1.90
12	3551.89			1.53
13	4196.47			0.72
14	4894.76			0.23
	Total	87.66	87.19	86.34

Table 3. Parameters and their uncertainties of the one-component free-α fits with $\chi^2_{\rm dof} \leqslant 1.13$

Constraint on $\alpha/\delta\alpha$	$T_{\rm dust}$ (K) min	$T_{\rm dust}$ (K) max	$\delta T_{\rm dust}$ (K)
$\geqslant$ 5.0	10.11	23.83	2.67
$\geqslant$ 6.7	10.12	22.69	1.95
$\geqslant$ 10.0	13.69	22.69	1.26

Constraint on $\alpha/\delta\alpha$	α min	α max	$\delta\alpha$
$\geqslant$ 5.0	1.08	4.71	0.91
$\geqslant$ 6.7	1.08	4.80	0.71
$\geqslant$ 10.0	1.24	3.13	0.31

Constraint on $\alpha/\delta\alpha$	τ $\times 10^{-5}$ min	τ $\times 10^{-5}$ max	$\delta\tau/\tau$ (per cent)
$\geqslant$ 5.0	0.33	46.15	62.83
$\geqslant$ 6.7	0.45	46.15	49.02
$\geqslant$ 10.0	0.61	46.15	23.25

One-component $\alpha = 1.7$ fits with $T_{\rm dust}/\delta T_{\rm dust} \geqslant 10$

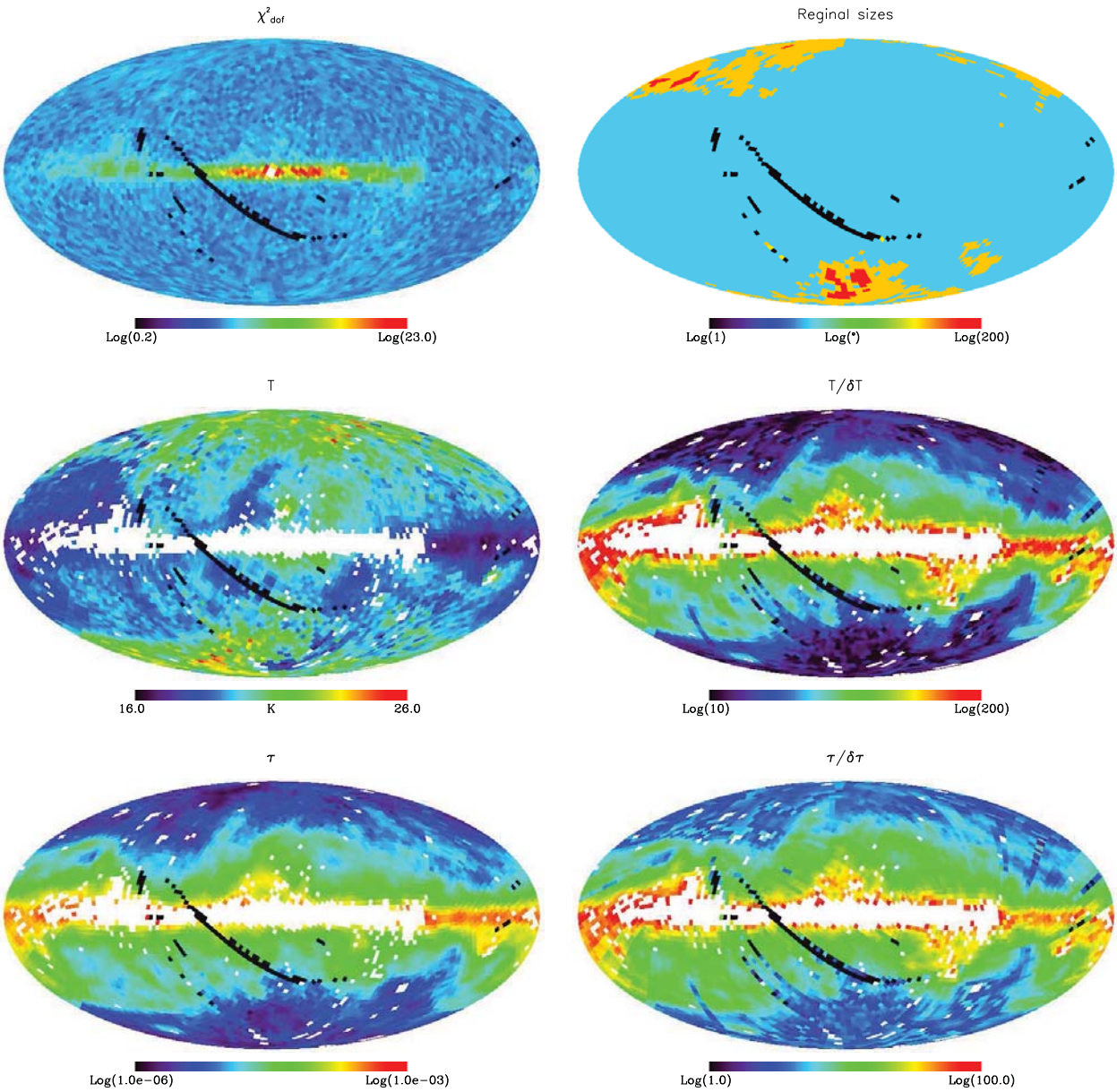

Figure 10. All-sky maps of $\chi^2_{\rm dof}$ (top left), spatial resolution (top right), $T_{\rm dust}$ (second left), $T_{\rm dust}/\delta T_{\rm dust}$ (second right), τ (bottom left), and $\tau/\delta\tau$ (bottom right) of the one-component $\alpha = 1.7$ fits that satisfy $T_{\rm dust}/\delta T_{\rm dust} \geqslant 10.0$ (from Liang 2011). These maps are in Galactic coordinate Mollweide projection with the Galactic centre at the centre and longitude increasing to the left. The regional size map shows that majority of the fits are at the 6.71-$\square^2$ level. In the parameter maps a pixel is masked in white if it corresponds to a χ^2 with less than 10 per cent probability. The group of black pixels that slant from the NEP to the SEP are positions where FIRAS did not provide data.

and emissivity spectral index for various levels of constraint on $\alpha/\delta\alpha$ are summarized in Table 3. In order to place adequate constraint on each parameter and to keep the regional sizes low, we adopt the $\alpha/\delta\alpha \geqslant 10.0$ constraint as our standard.

5 DISCUSSION

5.1 Comparing dust temperature predictions of different models

The crucial test to any model is comparison with reality. In this section, we present all-sky maps of dust temperature obtained from the literature and from our study. We argue that dust temperature distribution should generally follow the distribution of dust heating sources in the sky, and models that fail to do so are unphysical.

Fig. 14 presents dust temperature predictions by the two-component $\alpha = 2.0$ model of Reach et al. (1995), the two-

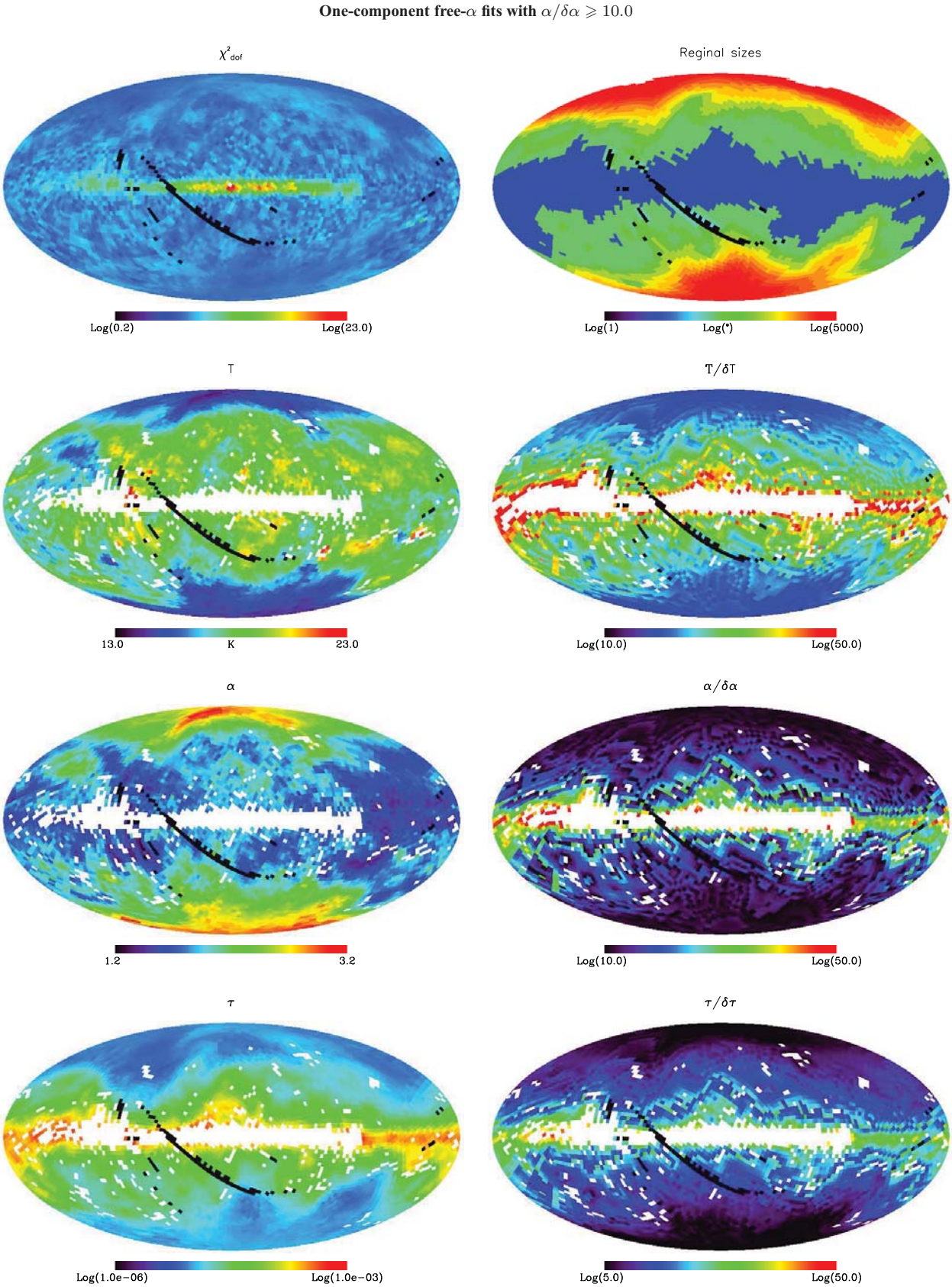

Figure 11. All-sky maps of $\chi^2_{\rm dof}$ (top left), spatial resolution (top right), dust temperature (second left), emissivity spectral index (third left), optical depth (bottom left), and their error estimates (right column) of the best-fitting one-component free-α fits that satisfies $\alpha/\delta\alpha \geqslant 10.0$ in Galactic coordinate Mollweide projection with the Galactic centre at the centre and longitude increasing to the left. In the parameter maps a pixel is masked in white if it corresponds to a $\chi^2_{\rm dof} \geqslant 1.13$. The group of black pixels that slant from the NEP to the SEP are positions where FIRAS did not provide data. Notice that dust temperature predictions at the Galactic polar caps are noticeably lower than the rest of the sky, consistent with our knowledge that the Galactic poles have fewer and cooler stars. Warm regions on the temperature map correspond to known emission sources (see text).

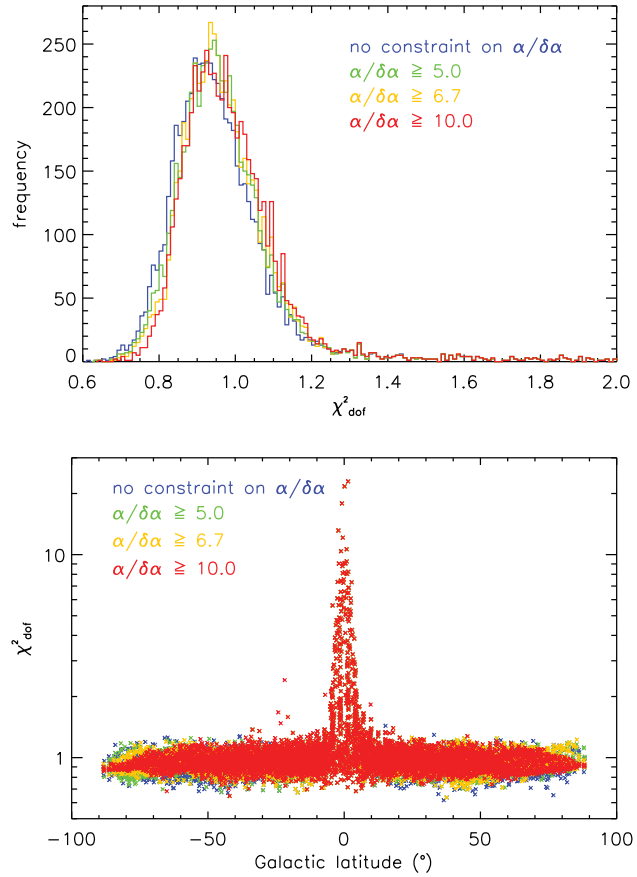

Figure 12. Upper: Distributions of $\chi^2_{\rm dof}$ from one-component free-α fits that use no constraint on any parameter and those that satisfy $\alpha/\delta\alpha \geqslant 5.0$, 6.7 and 10.0, respectively. This plot shows that the constraint has not altered the shape of the $\chi^2_{\rm dof}$ distributions drastically, and they all peak at ~ 0.95. Lower: $\chi^2_{\rm dof}$ vs. Galactic latitude. Notice that $\chi^2_{\rm dof}$ at high latitudes do not flare up as oppose to what happens when $\delta T_{\rm dust}/T_{\rm dust}$ requirements are imposed on the one-component fixed-α models, an indication that the free-α model is more adept at fitting various spectral shapes.

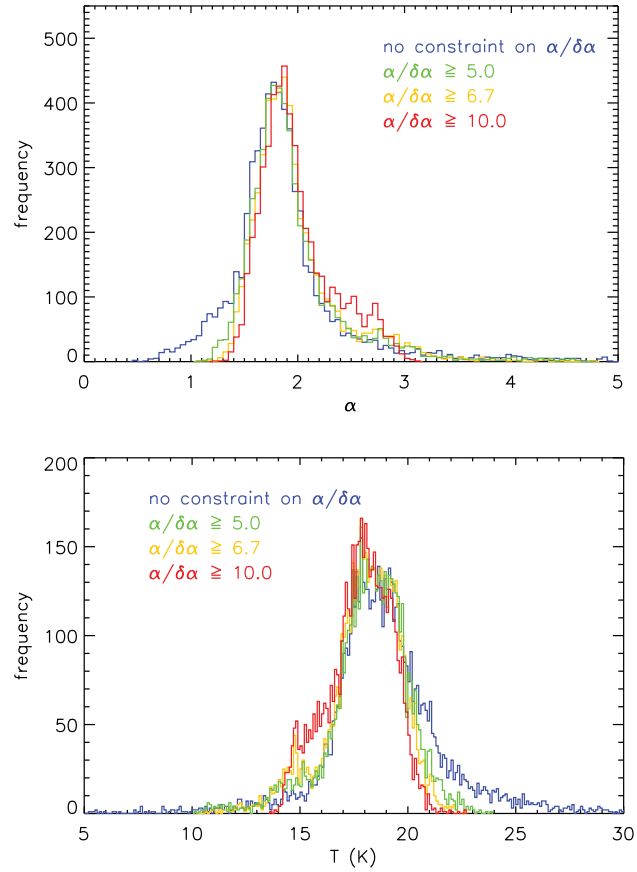

Figure 13. Distributions of α (top) and $T_{\rm dust}$ (bottom) of one-component free-α fits that use no constraint on any parameter and those that satisfy $\alpha/\delta\alpha \geqslant 5.0$, 6.7 and 10.0, respectively. Only those fits with $\chi^2_{\rm dof} \leqslant 1.13$ are included. Overall, the $\alpha/\delta\alpha$ requirement has the effect of moving α from below 1.5 to higher values, and the centres of the α distributions are found to be at 1.80, 1.83, 1.85 and 1.88, respectively. The plot of $T_{\rm dust}$ shows that distributions do not peak at a single value; the range of most popular temperatures is between 17 K and 20 K; imposing constraints on $\alpha/\delta\alpha$ smooths out the high-temperature points and effectively replaces them with values at or below 20 K.

component $\alpha_1 = 2.70$ and $\alpha_2 = 1.67$ Model #8 of Finkbeiner et al. (1999), the one-component $\alpha = 1.7$ model with $T_{\rm dust}/\delta T_{\rm dust} \geqslant 10.0$, and the one-component free-α model with $\alpha/\delta\alpha \geqslant 10.0$. The last two models are the ones derived in Section 4. We do not have Planck Collaboration's dust temperature predictions (Planck Collaboration 2011a), but since their one-component dust model has emissivity spectral index at 1.8, we use the temperature map of our one-component $\alpha = 1.7$ model to approximate their results.

Notice the difference in dust temperature predictions at the Galactic polar caps relative to lower latitude regions in these maps. In the first three cases, where emissivity spectral indices of the models are fixed, temperature predictions are higher around the Galactic polar caps than at lower latitudes. On the other hand, the free-α model predicts the polar caps to have the lowest temperature of the entire Galaxy. Consider that the Galactic poles have much fewer and cooler stars, we expect that dust temperature there be lower accordingly since fewer and weaker heating sources are present (Telesco & Harper 1980; Mathis et al. 1983; Stein & Soifer 1983; Cox, Krüegel & Mezger 1986; Mezger 1986; Boulanger & Pérault 1988; IRAS Explanatory Supplement 1988; Arendt et al. 1998; Leinert et al. 1998; Voges et al. 1999; Jones et al. 2002). Therefore, the temperature predictions of these fixed-α models are unphysical.

Moreover, since we have checked temperature predictions of models with spectral index at the range of most likely values between 1.4 and 2.6 (Liang 2011), and they all exhibit higher temperature at the Galactic polar caps than at lower latitudes, we suspect that such a phenomenon is an inherent artifact resulted from fixing the emissivity spectral index at a particular value.

In addition to predicting reasonable temperature distribution at the Galactic polar caps, the free-α model predicts regions with known heating sources to have higher temperature than their surrounding environment. For instance, we can identify, off the Galactic plane, high temperature regions that correspond to the Ophiuchus region, α Centauri, the Large Magellanic Cloud and the Orion region. At the Galactic plane, model predictions show that dust temperature decreases with increasing Galactocentric distance, consistent with previous observation by the DIRBE experiment (Sodroski et al. 1994). On top of this temperature gradience the temperature map shows the Outer Galaxy to be asymmetrically interspersed with strong infrared emission regions, such as NGC

7538 at $l = 111°$, Cas A at $111.°7 \lesssim l \lesssim 112.°1$, W3/4/5 at $132.°5 \lesssim l \lesssim 138.°5$, Cygnus region at $75° \lesssim l \lesssim 90°$, and the Gum Nebula at $187.°5 \lesssim l \lesssim 193.°5$. Becuase these regions contain complex emission sources in addition to dust, we mask them in all parameter maps to warn against any straightforward interpretation of the estimates.

Fig. 15 compares the normalized difference between data and intensity predictions by each of the aforementioned models at different Galactic latitudes. It shows that the free-α model is able to predict within 1-sigma of the data for the majority of the channels while the other models are less consistent at predicting close to measurement values across frequency and Galactic latitude. That the normalized differences of the $\alpha = 1.7$ model are comparable to those of the free-α model is a case in point for the limitation of a statistic, such as the normalized difference or the χ^2, in differentiating models: Here, the two models have about the same value for a statistic, but one of them is physically meaningful and the other is not.

5.2 Relation between dust temperature and emissivity spectral index

The existence of an anti-correlation between the emissivity spectral index and dust temperature has been a subject of debate in the last decade. Dupac et al. (2001, 2002, 2003) of the ProNaOS experiment reported evidence of the inverse correlation in their observation of M42, M17 and NGC891, Désert et al. (2008) of the Archeops experiment confirm the correlation on 304 Galactic point sources, Paradis (2010) confirm the existence of the correlation in two Hi-GAL fields at the Galactic plane, and Planck Collaboration (2011b) concluded that observation of objects in the Early Cold Core Catalogue were not consistent with a constant value of the spectral index over all temperature. On the other hand, Veneziani et al. (2010) did not find a clear inverse correlation between the two parameters in BOOMERANG's measurements of Galactic cirrus, Planck Collaboration (2011c) ruled against interpreting their results as evidence for an inverse correlation between dust temperature and emissivity spectral index due to majority of their data in the Rayleigh-Jeans tail of the modified blackbody spectrum, under which condition the two parameters become degenerate (Shetty et al. 2009a,b), and Planck Collaboration (2011a) derived dust temperature using a fixed value of the emissivity spectral index for the same reason.

The strongest argument for the existence of a temperature dependent power-law emissivity spectral index comes from laboratory measurements. Agladze et al. (1996) and Mennella et al. (1998) measured various silicate and carbonaceous grains that are considered close relatives of interstellar grains and found that value of the spectral index depended on temperature.

To test the possibility of an inverse correlation between emissivity spectral index and dust temperature in our data, we fit the best-fitting α and $T_{\rm dust}$ values of the free-α model with $\alpha/\delta\alpha \geqslant 10.0$ to the hyperbolic function $\alpha = 1/(\delta + \omega \cdot T_{\rm dust})$ and obtain $\delta = -0.510 \pm 0.011$ and $\omega = 0.059 \pm 0.001$ with a $\chi^2_{\rm dof} = 0.99$. The data and the best-fitting curve are presented in Fig. 16, and a summary of the best-fitting δ and ω for other levels of constraint on the fits are presented in Table 4. Indeed, the exact functional form of the temperature-dependent spectral index cannot be established by our data alone. However, that a physically sensible fit to the all-sky data requires a free-α model and that a hyperbolic function fits the α and $T_{\rm dust}$ values well give strong support to the anti-correlation between the emissivity spectral index and dust temperature.

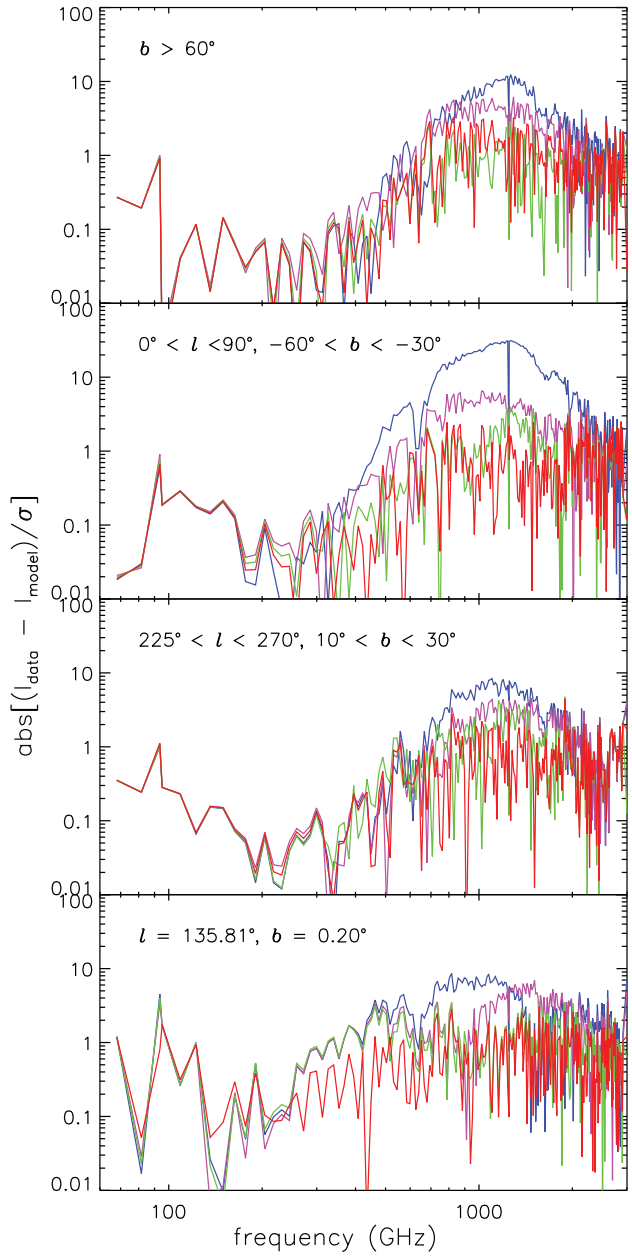

Figure 15. Normalized difference between the averaged 214-channel dust spectra and model predictions. Blue represents the two-component $\alpha = 2.0$ model of Reach et al. (1995); magenta represents Model #8 of Finkbeiner et al. (1999); green represents the one-component $\alpha = 1.7$ model of Liang (2011); and red represents the one-component free-α model of this work. The normalized differences are obtained by first subtracting model predictions from each 7° dust spectra, next dividing the results by measurement uncertainties, then averaging the normalized difference, and finally taking the absolute value. These plots show that the free-α model is able to predict within 1-sigma of the data for the majority of the channels at difference Galactic latitudes while the other models are less consistent at predicting close to measurement values across frequency and Galactic latitude.

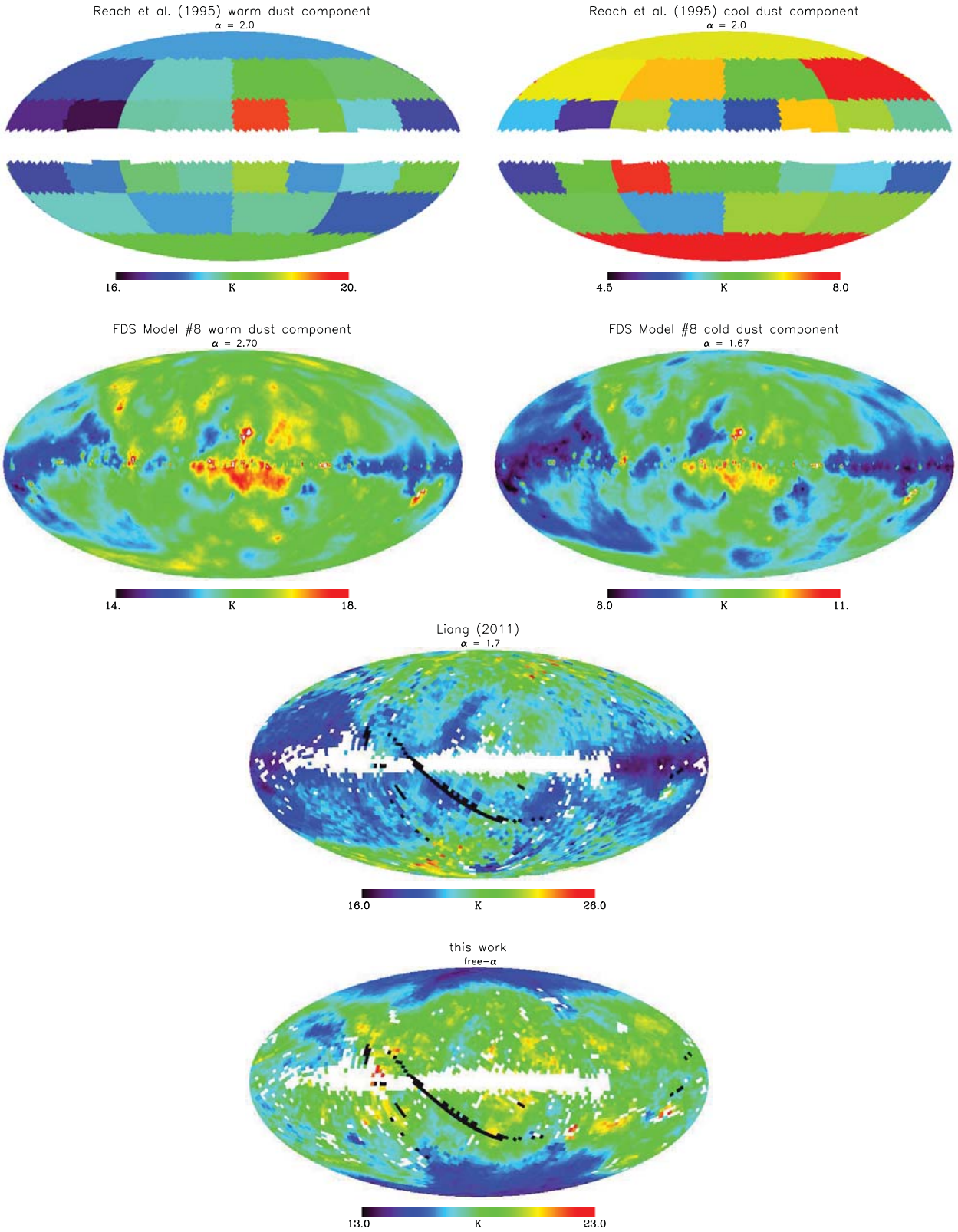

Figure 14. Dust temperature maps by the two-component $\alpha = 2.0$ model of Reach et al. (1995) (first row), the two-component $\alpha_1 = 2.70$ and $\alpha_2 = 1.67$ Model #8 of Finkbeiner et al. (1999) (second row), the one-component $\alpha = 1.7$ model with $T_{\rm dust}/\delta T_{\rm dust} \geqslant 10$ of Liang (2011) (third row), and the one-component free-α model with $\alpha/\delta\alpha \geqslant 10$ of this work(last row). Data of the Reach model were obtained from their manuscript; the Galactic plane of both maps have been masked due to incomplete data for the region. Data of the Finkbeiner model were generated from their IDL code "predict_thermal.pro." Pixels in both the $\alpha = 1.7$ and the free-α maps are masked in white if they correspond to a $\chi^2_{\rm dof} > 1.13$. Notice that the fixed-α models represented in the first three rows predict higher temperature at the Galactic polar caps than at lower latitudes. On the contrary, the free-α model (last row) predicts the Galactic polar caps to have the lowest temperature of the entire Galaxy. Predictions of the fixed-α models are unphysical, since Galactic polar caps are known to have fewer and cooler stars, and the dust temperature must be accordingly lower where few and weak heating sources are present.

Table 4. Best-fitting parameters to the relation $\alpha = 1/(\delta + \omega \cdot T_{\rm dust})$ between emissivity spectral index and dust temperature

constraint on fits	δ	ω	number of data points	$\chi^2_{\rm dof}$
no constraint	-0.305 ± 0.014	0.048 ± 0.001	5421	0.72
$\alpha/\delta\alpha \geqslant 5.0$	-0.399 ± 0.013	0.053 ± 0.001	5386	0.83
$\alpha/\delta\alpha \geqslant 6.7$	-0.441 ± 0.012	0.055 ± 0.001	5357	0.88
$\alpha/\delta\alpha \geqslant 10.0$	-0.510 ± 0.011	0.059 ± 0.001	5305	0.99

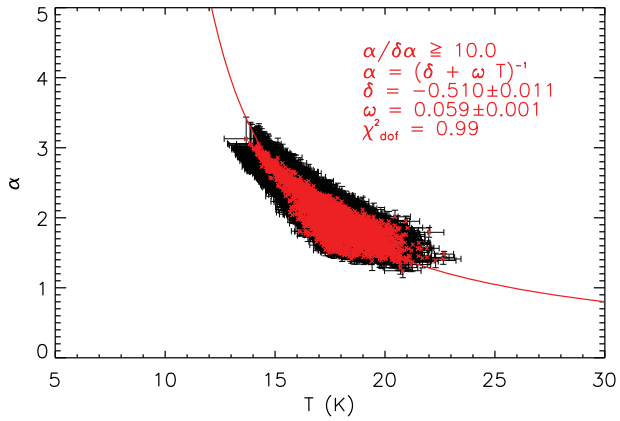

Figure 16. Scatter plot of the best-fitting α and $T_{\rm dust}$ values. The red dots represent values of α and $T_{\rm dust}$ from fits that satisfy $\alpha/\delta\alpha \geqslant 10.0$. Error bars of α and $T_{\rm dust}$ are plotted in black, and are used in the curve fitting process. Best-fitting hyperbolic function in the form of $\alpha = 1/(\delta + \omega \cdot T_{\rm dust})$ is represented by the red curve. The best fitting parameters for various levels of constraint on $\alpha/\delta\alpha$ are summarized in Table 4. Only fits with $\chi^2_{\rm dof} \leqslant 1.13$ are included. That the hyperbolic function is a good fit to our α and $T_{\rm dust}$ values supports the argument for an anti-correlation between the two parameters.

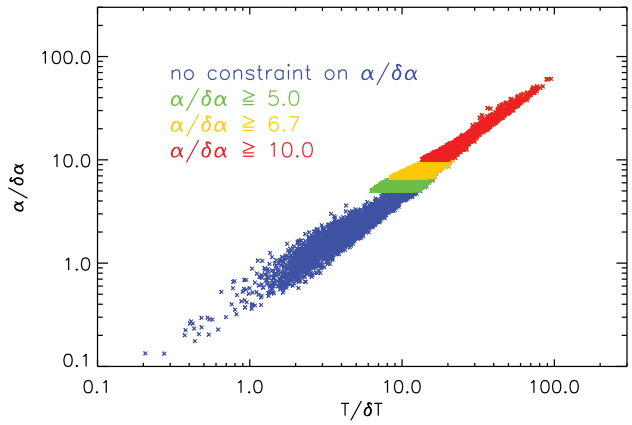

Figure 17. Scatter plot of $\alpha/\delta\alpha$ and $T_{\rm dust}/\delta T_{\rm dust}$. The blue, green, yellow and red data points represent values of $\alpha/\delta\alpha$ and $T_{\rm dust}/\delta T_{\rm dust}$ from fits that use no constraint on any parameter and those that satisfy $\alpha/\delta\alpha \geqslant 5.0$, 6.7 and 10.0, respectively. Only fits with $\chi^2_{\rm dof} \leqslant 1.13$ are included. These distributions show that the uncertainty on α and $T_{\rm dust}$ can both be reduced at the same time, while α is more susceptible to errors than $T_{\rm dust}$.

One can be assured that the observed correlation between emissivity spectral index and dust temperature in our data is intrinsic rather than from noise. In 2009, Shetty et al. showed that the accuracy of parameter estimation depends on the wavelength range of the spectra used in model fitting. They show that for dust temperature $\leqslant 20$ K, fits using spectra at 100–600 μm are not sensitive to noise. However, if 40 K $\leqslant T_{\rm dust} \leqslant$ 80 K, a 5 per cent noise in a data set of different $T_{\rm dust}$ and the same α may generate a pattern in the best-fitting α vs. $T_{\rm dust}$ plot that can be confused with a true anti-correlation in the two parameters. Since our spectra, coming at 100–4400 μm, well sample the Rayleigh-Jeans tail of the peak of the ~ 20 K modified blackbody spectrum, our best-fitting parameters are good approximates of the true values.

As the quality of data improves, the free-α model allows us to pinpoint the values of α and $T_{\rm dust}$ with greater accuracy. In Fig. 17 we present $\alpha/\delta\alpha$ vs. $T_{\rm dust}/\delta T_{\rm dust}$ of the all-sky collections of fits with different amounts of constraint on $\alpha/\delta\alpha$. It shows that the uncertainty in α and $T_{\rm dust}$ are directly proportional, while α is more susceptible to errors than $T_{\rm dust}$. That is, with more sensitive data one will be able to reduce uncertainty in α and $T_{\rm dust}$ at the same time.

6 CONCLUSIONS

We have examined models of interstellar dust thermal emission at far-infrared and millimeter wavelengths. Starting with deducing a new and improved version of dust spectra from FIRAS calibrated measurements and unifying them with measurements of the DIRBE and the *WMAP*, one-component dust models with fixed and variable emissivity spectral index are fit to 6063 214-channel spectra at fixed and variable spatial resolutions.

We show that the free-α model can predict more dust temperature than models with fixed emissivity spectral index. Starting with the knowledge that the Galactic polar caps have fewer and cooler stars, which means fewer and weaker heating sources for interstellar dust, dust temperature is expected to be lower at the Galactic polar caps than at lower latitudes. Among all-sky dust models found in the literature and the one-component dust models constructed in our study, we demonstrate that only the free-α model passes this test. All fixed-α models predict higher temperatures at the Galactic polar caps than at lower latitudes.

Our best dust model is the one-component free-α model with $\alpha/\delta\alpha \geqslant 10.0$. It fits dust spectra over 86 per cent area of the full sky. Dust temperature is predicted to be $13.69 - 22.69$ (± 1.26) K, emissivity spectral index to be $1.2 - 3.1$ (± 0.31), and optical depth to range $0.61 - 46.15 \times 10^{-5}$ with a 23.25 per cent uncertainty. This model has the 7° angular resolution of FIRAS and uses spatial averaging at high latitudes. The model supports the anti-correlation between emissivity spectral index and dust temperature. Fitting the relation $\alpha = 1/(\delta + \omega \cdot T_{\rm dust})$ to the α and T values, we obtain $\delta = -0.510 \pm 0.011$ and $\omega = 0.059 \pm 0.001$.

The free-α model can be used to remove dust contamination in CMB measurements. Our results also serve as an all-sky extended-frequency-range reference for other experiments. With higher resolution data sets, such as those from Planck, one will be able to

improve resolution and further reduce the uncertainty of the model parameters.

ACKNOWLEDGMENTS

Some of the results in this paper have been derived using the HEALPix (K.M. Górski et al., 2005, ApJ, 622, p759) package.

The author ZL thanks very much Professor Charles Bennett for the enlightening discussions, intuitive guidance, and generous support, all of which made this work possible. ZL also thanks Drs. Janet Weiland, David Larson and Domenico Tocchini-Valentini for very helpful discussions.

REFERENCES

Agladze N.I., Sievers A.J., Jones S.A., Burlitch J.M., Beckwith S.V.W., 1996, ApJ, 462, 1026
Arendt R.G. et al., 1998, ApJ, 508, 74
Bennett C.L. et al., 2003a, ApJ, 583, 1.
Bennett C.L. et al., 2003b, ApJS, 148, 97
Boggess N.W. et al., 1992, ApJ, 397, 420
Boulanger F., Pérault M., 1988, ApJ, 330, 964
Boulanger F., Abergel A., Bernard J.P., Burton W.B., Desert F.X., Hartmann D., Lagache G., Puget J.L., 1996, A&A, 312, 256
Calabretta M.R., Greisen E.W., 2002, A&A, 395, 1077-1122
Calabretta M.R., Roukema B.F., 2007, MNRAS, 381, 865
Chan F.K., O'Neill E.M., 1975, EPRF Technical Report 2 - 75 (CSC). Computr Science Corporation, Silver Springs, Maryland
Cox P., Krüegel E., Mezger P. G., 1986, A&A, 155, 380
de Vaucouleurs G., Buta R., 1983, AJ, 88, 939
Désert F.X. et al., 2008, A&A, 481, 411
COBE Diffuse Infrared Background Experiment (DIRBE) Explanatory Supplement. 1998, in Hauser M.G., Kelsall T., Leisawitz D., Weiland J., eds, COBE Ref. Pub. No. 98-A, Greenbelt, MD: NASA/GSFC
Draine B.T., Lee H.M., 1984, ApJ, 285, 89
Dupac X. et al., 2001, ApJ, 553, 604
Dupac X. et al., 2002, A&A, 392, 691
Dupac X. et al., 2003, A&A, 404, L11
Finkbeiner D.P., Davis M., Schlegel D.J., 1999, ApJ, 524, 867
Finkbeiner D.P., Davis M., Schlegel D.J., 2000, ApJ, 544, 81
COBE Far Infrared Absolute Spectrophotometer (FIRAS) Explanatory Supplement. 1997, in Brodd S., Fixsen D.J., Jensen K.A., Mather J.C., Shafer R.A., eds, COBE Ref. Pub. No. 97-C. Greenbelt, MD: NASA/GSFC
Fixsen D.J., 2009, ApJ, 707, 916
Fixsen D.J., Dwek, E., 2002, ApJ, 578, 1009
Fixsen D.J., Mather J.C., 2002, ApJ, 581, 817
Fixsen D.J. et al., 1994a, ApJ, 420, 445
Fixsen D.J. et al., 1994b, ApJ, 420, 457
Fixsen D.J., Cheng E.S., Gales J.M., Mather J.C., Shafer R.A., Wright E.L., 1996, ApJ, 473, 576
Fixsen D.J. et al., 1997b, ApJ, 490, 482
Fixsen D.J., Dwek E., Mather J.C., Bennett C.L., Shafer R.A., 1998, ApJ, 508, 123
Gold B. et al., 2009, ApJS, 180, 265
Gorjian V., Wright E.L., Chary R.R., 2000, ApJ, 536, 550
Górski K.M., Hivon E., Wandelt B.D., 1999, in Banday A.J., Sheth R.S., Da Costa L., eds, Proceedings of the MPA/ESO Cosmology Conference, Evolution of Large-Scale Structure. Ipskamp, NL, 37
Górski K.M., Hivon E., Banday A.J., Wandelt B.D., Hansen F.K., Reinecke M., Bartelmann M., 2005, ApJ, 622, 759
Hauser M.G. et al., 1998, ApJ, 508, 25
Hill R.S. et al., 2009, ApJS, 180, 246
Hinshaw G. et al., 2003, ApJS, 148, 63
Hinshaw G. et al., 2007, ApJS, 170, 288
Hinshaw G. et al., 2009, ApJS, 180, 225
IRAS Catalogs and Atlases: Explanatory Supplement. 1988, in Beichman C.A., Neugebauer G., Habing H.J., Clegg P.E., Chester T.J., eds, Washington, DC: GPO.
Jarosik N. et al., 2003, ApJS, 145, 413
Jarosik N. et al., 2007, ApJS, 170, 263
Jones L.V., Elston R.J., Hunter D.A., 2002, ApJ, 124, 2548
Kelsall T. et al., 1998, ApJ, 508, 44
Lagache G., Abergel A., Boulanger F., Puget J.L., 1998, A&A, 333, 709
Leinert Ch. et al., 1998, A&AS, 127, 1
Liang Z., 2011, PhD thesis, Johns Hopkins University
Mather J.C., 1982, Opt. Eng., 21, 769
Mather J.C., Toral M. & Hemmati H. 1986, Appl. Opt., 25, 2826
Mather J.C. et al., 1990, ApJ, 354, L37
Mather J.C., Fixsen D.J. & Shafer R.A., 1993, Proc. SPIE, 2019, 168
Mather J.C. et al., 1994, ApJ, 420, 439
Mather J.C., Fixsen D.J., Shafer R.A., Mosier C., Wilkinson D.T., 1999, ApJ, 512, 511
Mathis J. S., Mezger P. G., Panagia N., 1983, A&A, 128, 212
Mennella V., Brucato J.R., Colangeli L., Palumbo P., Rotundi A., Bussoletti E., 1998, ApJ, 496, 1058
Mezger P.G., 1986, Astrophys. & Space Sci., 128, 111
O'Neill E.M., Laubscher R.E., 1976, NEPRF Technical Report 3 - 76 (CSC). Computer Sciences Corportion, Silver Springs, Maryland
Page L. et al., 2003, ApJS, 148, 39
Paradis D. et al., 2010, A&A, 520, 8
Planck Collaboration, 2011a, A&A, 536, 19
Planck Collaboration, 2011b, A&A, 536, 23
Planck Collaboration, 2011c, A&A, 536, 24
Reach W.T. et al., 1995, ApJ, 451, 188
Schlegel D.J., Finkbeiner D.P., Davis, M., 1998, ApJ, 500, 525
Shetty R., Kauffmann J., Schnee S., Goodman A.A., 2009, ApJ, 696, 676
Shetty R., Kauffmann J., Schnee S., Goodman A.A., Ercolano B., 2009, ApJ, 696, 2234
Silverberg R.F., Hauser M.G., Boggess N.W., Kelsall T.J., Moseley S.H., Murdock T.L., 1993, Proc. SPIE, 2019, 180
Sodroski T.J. et al., 1994, ApJ, 428, 638
Stein W.A., Soifer B.T., 1983, ARA&A, 21, 177
Telesco C.M., Harper, D.A., 1997, ApJ, 235, 392
Veneziani M. et al., 2010, ApJ, 713, 959
Voges W. et al., 1999, A&A, 349, 389
White R.A., Stemwedel S.W., 1992, ASPC, 25, 379
Wilkinson Microwave Anisotropy Probe *WMAP*: Five-Year Explanatory Supplement. 2008, in Limon M. et al., eds, Greenbelt, MD:NASA/GSFC
Wright E.L. et al., 1991, ApJ, 381, 200

This paper has been typeset from a TEX/ LATEX file prepared by the author.